LITHOS 414-415 (2022) 106620

Contents lists available at ScienceDirect

LITHOS

journal homepage: www.elsevier.com/locate/lithos

Crystallisation and fast cooling of the (meta)gabbro from the Chenaillet ophiolite (Western Alps): In-situ U—Pb dating of zircon, titanite, monazite and xenotime in textural context

Christian Nicollet [*], Jean-Louis Paquette, Emilie Bruand, Valérie Bosse, Inês Pereira

Laboratoire Magmas et Volcans, Université Clermont Auvergne, CNRS, IRD, OPGC, F-63000 Clermont-Ferrand, France

ARTICLE INFO

Keywords:
Alps
Chenaillet ophiolite
Metagabbro
Fast cooling
LA-ICPMS in situ dating
Accessory minerals

ABSTRACT

The Chenaillet ophiolite, South of Montgenèvre (France), represents a preserved portion of the alpine ocean. The gabbros form lenticular bodies 50 to 200 m thick and a few hundreds of meters wide. They are intrusive in the serpentinites and often overlain by pillow-lavas. Plagiogranite/albitite veins are rare and volumetrically negligible. The petrology of the gabbro s.s. show great details of the progressive cooling of the massif, clinopyroxene are often rimmed by brown to green amphibole +/− ilmenite/titanite. Thermometry on these amphibole assemblages indicates a retrograde temperature evolution from late magmatic to subsolidus, between 950 and 900 °C, 800–750 °C, 600–500 °C. In a shear zone, a string of titanite associated with monazite and xenotime +/− ilmenite is located in a millimetric greenschist layer whose temperature is estimated at 600–550 °C. Accessories chemistry in this sample allowed in situ dating by LA-ICPMS on thin section in textural context. In the same sample, we performed U—Pb zircon dating, constraining the magmatic age, as well as U—Pb monazite, xenotime and titanite dating for the metamorphic evolution. In a Tera-Wasserburg diagram, monazite, xenotime and titanite yield 161.3 +/− 4.0 Ma, 161.5 +/− 2.4 Ma and 158.4 +/− 2.3 Ma lower intercept ages, respectively, while the zircon from the same sample indicates an age of 161.0 +/− 0.8 Ma. Finally, zircon dated in an albitite vein also yields a 161.8 ± 1.7 Ma age. These similar ages within the analytical uncertainties show that magmatism and metamorphism were concomitant. Thermal modelling predicts that a 150 m thick gabbroic massif crystallizes in a few hundred years and cools down in several thousand years. This is consistent with the ages reported in our study showing that the retrograde metamorphism in this massif records fast cooling. The development of this retrograde metamorphism required multiple fluid infiltrations during cooling. In the studied samples, 4 types of titanites could be distinguished based on their chemistries. 3 types variously depleted in REE are interpreted as related to water-driven fluids while another type has up to 10% REE, Y and Nb and suggest a possible felsic source. The two potential sources of water promoting this fast cooling are sea water-derived fluids and magmatic fluids exsolved from felsic veins.

1. Introduction

The Chenaillet ophiolite, South of Montgenèvre, in the Western Alps is one of the very well-preserved portions of the alpine ophiolites, which represent remnants of the Tethys oceanic domain (Fig. 1). The alpine Tethys developed as a rather narrow basin, with a maximum width of less than 800 km and a very low spreading rate. It formed during a short-lived phase of magmatism between 165 Ma and 155 Ma (Manatschal and Müntener, 2009; McCarthy et al., 2021; Tribuzio et al., 2016). Alpine ophiolites constitute a heterogeneous lithosphere similar to that formed at slow/ultra-slow spreading ridges or ocean-continent transition. They are mainly composed of variably serpentinised mantle peridotites and irregularly distributed magmatic rocks composed of gabbroic lenses and discontinous basaltic cover. Gabbros, troctolite, diorite and albitite are commonly found in alpine ophiolites and are thought to be the result of fractional crystallisation of evolving melts and/or the interaction between a fractionating crystal mush with an external evolved melt (Rampone and Sanfilippo, 2021). Basaltic dykes are rare and the sheeted dyke complex associated with classical Penrose-type model of ophiolites is lacking. Overall, these magmatic rocks have a geochemical affinity of MORB, similar to that of oceanic basalts and kilometre-scale detachment faults accommodated the exhumation of mantle rocks and gabbros to the

---

[*] Corresponding author.
E-mail address: christian.nicollet@uca.fr (C. Nicollet).

https://doi.org/10.1016/j.lithos.2022.106620
Received 20 September 2021; Received in revised form 28 January 2022; Accepted 31 January 2022

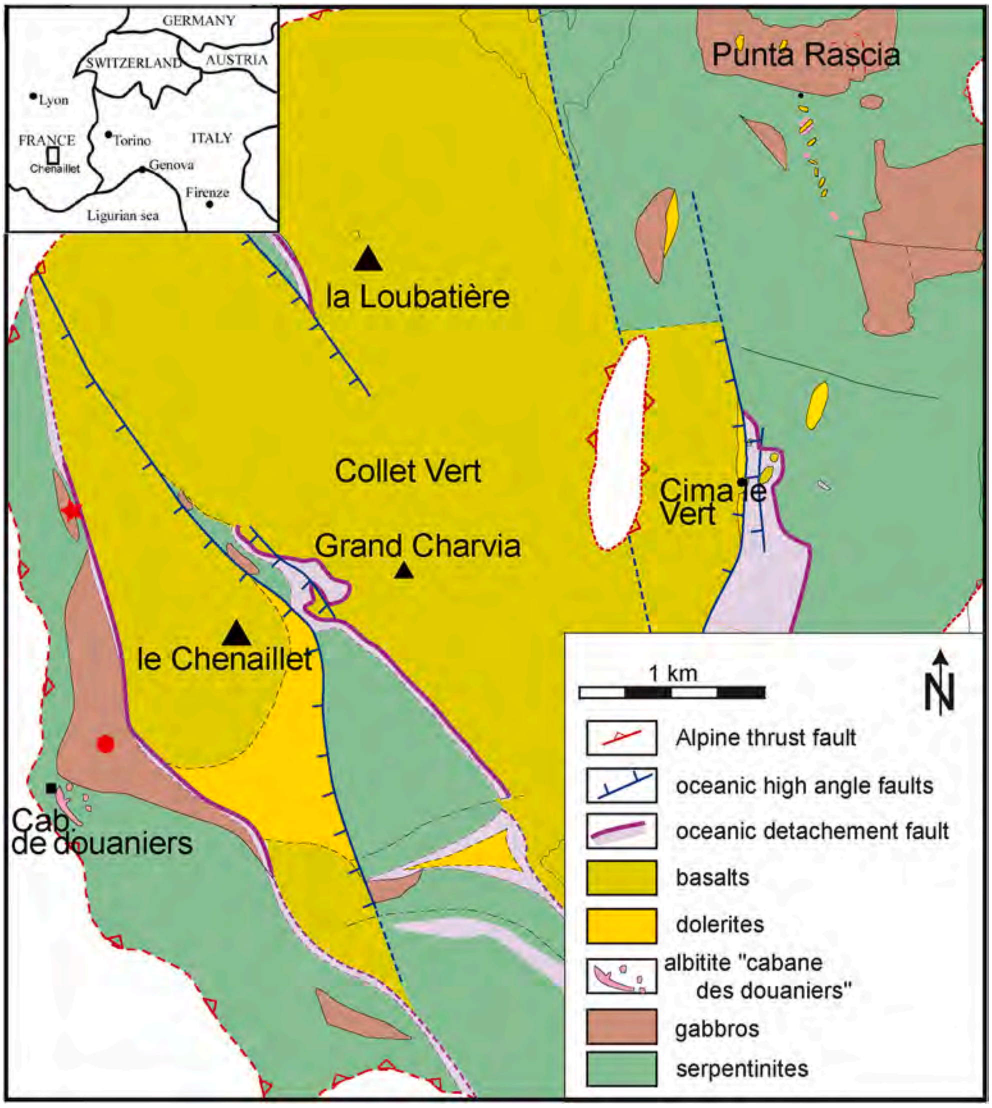

Fig. 1. Geological map of the Chenaillet Ophiolite; simplified after Manatschal et al. (2011). Red spot: samples CH1 and CH4; red star: sample CH3. (For interpretation of the references to colour in this figure legend, the reader is referred to the web version of this article.)

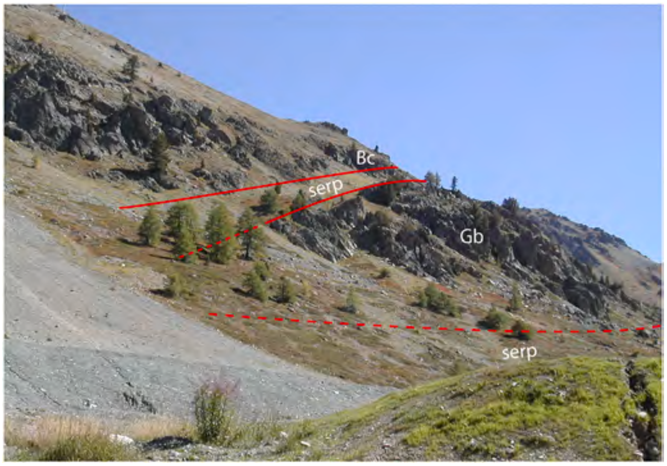

Fig. 2. Gabbroic lens (Gb) of Mont Chenaillet. It is intrusive in serpentinites (serp), themselves covered by pillow basalts (Bc) on the western flank of the NW ridge of the Mont Chenaillet. Sample CH3 comes from the top of this lens. View from les Prés du Gondran.

sea floor. Some of these ophiolites are formed in the mantle of the continental margin and represent ocean-continent transition (OCT) while others constitute intra-oceanic domains (Manatschal and Müntener, 2009).

According to these authors, the Chenaillet ophiolite would represent an intra-oceanic domain. The massif of the Mont Chenaillet has overlapped the continental crust and displays only weak effects of alpine deformation and metamorphism related to the alpine collision at 33 Ma. This ophiolite is characterized by the occurrence of exhumed serpentinised mantle, intruded by small lenses of gabbros; a voluminous volcanic complex is fed by rare dykes (Mevel et al., 1978; Bertrand et al., 1982; Bertrand et al., 1987; Caby, 1995; Chalot-Prat, 2005; Manatschal et al., 2011 and reference therein). In the Chenaillet massif, various rock types such as gabbros, troctolite, diorite and albitite, have been dated (Costa and Caby, 2001; Chalot-Prat, 2005; Desmurs et al., 2002, for a review see Li et al., 2013). These latter suggested that the troctolites and albitites crystallised synchronously at about 165 Ma, which is consistent with age estimates of the mantle exhumation of the Alpine Tethys ocean after continental breakup (Manatschal and Müntener, 2009). This date is also consistent with the middle-bathonian age of the oceanic sediments of the neighbouring Lago Nero-Replatte unit which is considered to be the base of the sedimentary succession associated with the ophiolite

Fig. 3. Contact between an ophitic-textured gabbro and a microgabbro. The contact is sharp and could represent intrusive contact, indicative of a (possible) local replenishment of the magmatic lens.

body (Cordey and Bailly, 2007).

While previous geochronological works focused on the emplacement and crystallisation of magmatic rocks, the present study aims at distinguishing the magmatic event by analyzing the zircons of an albitite vein (CH4) and of a (meta-)gabbro (CH1) from the cooling event by analyzing the various REE-bearing minerals associated with the metamorphism of this metagabbro. Using U—Pb and trace elements results, we discuss the cooling rate of this gabbro massif by comparing ages obtained with a simple thermal modelling, and conclude by using the chemical signature of titanite on the nature of the fluids which can contribute to this cooling.

2. Geological background

On the SW ridge (crest) of Mont Chenaillet, a massif of gabbro forms a lenticular body from (of) 50 to 150 m thick and nearly 2 km long. It is intrusive into the serpentinites and sometimes directly overlain by the pillow lavas (Fig. 2). According to Manatschal et al. (2011), the contact between the serpentinites/gabbros and the lavas is defined by a detachment fault along which the serpentinites/gabbros were exhumed at the seafloor level before the emplacement of lavas flows. The latter are fed by a few basaltic dikes that crosscut both gabbros and serpentinites: The voluminous volcanic complex was built later than the gabbroic complex: basalts and gabbros have been suggested to originate from the same magma source, but the plutonic system do not contribute to the volcanic complex (Bertrand et al., 1987).

The lithology of this gabbro massif itself is mostly composed of coarse-grained clinopyroxene-rich gabbros but other lithologies such as troctolites, diorites and albitites, can be found. Troctolites (or more accurately metatroctolites) and olivine gabbros mainly occur at the base of the unit: the continuous transition between gabbros - olivine gabbros and troctolites suggests that these rocks crystallised synchronously. Dolerites also occur as rare dykes or small massifs. Finally, albitites form centimetric to metric dikes within the gabbro massif. One exception is a small decametric massif in the serpentinites, at « la Cabane des Douaniers » locality, which has been dated by Li et al. (2013). The entire ophiolitic massif recorded an oceanic seafloor metamorphism prior to a low grade alpine metamorphism (Bertrand et al., 1987; Mevel et al., 1978).

3. Lithology and petrography of the gabbroic rocks

Petrography of the gabbros stricto sensu is diversified. The magmatic ophitic textures is locally affected by high temperature ductile shearing (Caby, 1995) and the deformation is heterogeneous. Gabbros are coarse- to fine-grained and the variation in crystal size can be sharp (Fig. 3). These sharp boundaries could indicate possible replenishments or re-injections of magma at different stages of the gabbro crystallisation/ cooling evolution.

Here we describe three typical samples of gabbros s.s. and one metatroctolite representative of the massif. The samples CH1 and CH4 were collected from the SW ridge of the Mont Chenaillet, on the centre of the gabbro lens (44°53′53“ N; 6°44’3.35”E); the CH3 sample comes from the northern margin of the gabbro massif, in contact with the serpentinites, next to an oceanic detachment fault (44°54′26.5“ N; 6°43’48.55”E; Fig. 1). In the following, we only describe the petrography of the metatroctolite (CH5) but will not present chemical analyses related to it. This sample is important to understand and discuss the fluid origins affecting the gabbro massif. The mineralogical assemblages are listed in the Supplementary data_1.

Sample CH4: The rock is an undeformed gabbro crosscuts by a centimetric thick vein of albitite. The gabbroic part of the sample is coarse-grained with an ophitic texture. Clinopyroxene and plagioclase are the main minerals and are centimetric in size. Clinopyroxene are sometimes rimmed by a thin corona of brown amphibole (<0.1 mm).

The albititic vein present in the sample has an irregular and diffuse contact with the gabbro, suggesting that the melt feeding the felsic vein intruded the gabbro when it was not completely solidified. It is mostly made up of albitic plagioclase, apatite, ilmenite, rare epidote and chlorite. Brown-green amphibole crystals representing the only ferromagnesian mineral (Table 1) in this vein, are rare. Some euhedral and cracked zircon crystals of several hundred micrometers in size also occur (cathodoluminescence image in Fig. 11b). Late fractures filled with epidote and actinolite crosscut the rock.

Sample CH3: This sample is collected on the strongly deformed edge of the gabbro at the top of the lens which is in contact with the serpentinites, just below the oceanic detachment fault (near section I of Manatschal et al., 2011; Figs. 2 and 4*)*. The gabbro has been metamorphosed at granulite/amphibolite conditions as indicated by dark brown amphibole as the main ferromagnesian mineral and minor clinopyroxene. Centimetric porphyroclasts of brown amphibole are wrapped by a well-developed foliation (Fig. 4). This brown amphibole is deformed and mantled by light brown and green coronitic amphiboles. The light brown amphiboles are associated with ilmenite (Fig. 5), while the green amphiboles are associated with titanite (Fig. 6). Rutile exsolution lamellae has been observed within titanite and are related to the replacement of ilmenite. Finally, another generation of titanite occurs in late fractures. Plagioclase is often recrystallised in an aggregate of fine crystals of sodium-rich compositions close to albite (Table 1). When present, clinopyroxene is also surrounded by a corona of dark brown to light brown and green zoned amphiboles, similar to that of the surrounding amphiboles. Contrary to the undeformed CH4 sample, the abundance of amphiboles highlights that this sample is heavily amphibolitized.

Sample CH1: The rock is affected by anastomosed high temperature ductile shear zones marked by the development of a pronounced metamorphic layering, consequently the rock can be defined as metagabbro. The mineralogical association is mainly made up of clinopyroxene, brown to green amphibole and plagioclase rich in albitic end member (Table 1). Accessory minerals are apatite, ilmenite, titanite (Fig. 8), cracked zircon crystals (cathodoluminescence image in Fig. 12a) and a few monazite (Fig. 8c) and xenotime crystals (Fig. 8d). It is worth noting that feldspar is black with a dusty appearance: it is replaced by a fine aggregate of epidote, albite-oligoclase, +/−chlorite corresponding to the prehnite – pumpellyite metamorphic facies. The metagabbro exhibits coronitic texture similar to CH3 sample. However more complex textures can also be observed (Fig. 7). From clinopyroxene to plagioclase, clinopyroxene–brown amphibole symplectites replace the porphyroclasts of magmatic clinopyroxene (CpxMag). This pyroxene is recrystallised into an aggregate of neoblastics clinopyroxene with brown hornblende (Cpx2 + bHbl) in a granulite metamorphic

Table 1
Electron microprobe analyses of the major elements of amphibole – plagioclase and geothermometry; H-B: Holland and Blundy (1994), edenite-tremolite calibration. Act-String, Pl-String: actinolite and plagioclase of the string of titanite +/− ilmenite; Cpx: clinopyroxene; BHbl, LbHbl, GHbl: brown, light brown, green hornblende; Cor: coronitic mineral. Preferred temperature estimates are in bold. na: Purtika thermometer not applied on greenschist facies amphiboles.

sample	**Metagabbro Ch1**													**Metagabbro Ch3**				
Figure	**8**													**6**				
mineral	Act-String	Pl-String	Act-String	Pl-String	Act-String	Pl-String	Cpx	BHbl-Cor	BHbl-Cor	BHbl	GHbl-Cor	GHbl-Cor	BHbl-Cor	ActCor	GHblCor	PlCor	ActCor	BHbl
SiO2	53.19	64.19	53.99	64.13	54.04	65.44	53.54	47.20	44.85	45.73	48.83	46.88	48.56	52.11	46.20	68.230	51.73	44.05
TiO2	0.57	0.00	0.50	0.00	0.41	0.03	0.21	2.25	2.66	2.62	0.46	0.39	1.90	0.08	0.36	0.020	0.32	2.97
Cr2O3		0.00		0.01		0.01	0.61				0.34	0.56				0.000		
Al2O3	3.00	22.58	2.63	22.54	2.64	21.53	1.46	7.86	8.86	9.10	6.63	10.71	7.61	3.04	7.64	20.890	3.54	9.37
FeO	9.93	0.11	9.29	0.10	8.99	0.11	3.87	10.46	11.76	11.33	11.67	10.90	8.77	17.55	20.68	0.220	16.21	14.50
MnO	0.24	0.02	0.29	0.00	0.22	0.00	0.23	0.24	0.28	0.25	0.17	0.26	0.19	0.30	0.29	0.000	0.27	0.38
MgO	17.90	0.02	18.38	0.00	18.57	0.00	15.65	14.73	13.74	15.13	15.04	14.33	16.50	12.30	8.72	0.010	12.97	12.95
CaO	11.42	3.77	11.07	3.68	11.36	2.84	23.63	11.36	11.39	10.93	12.54	12.30	12.15	12.50	11.76	1.610	12.15	9.89
Na2O	0.83	9.51	0.75	9.48	0.71	9.93	0.37	1.82	2.15	2.32	1.33	2.15	1.77	0.23	1.44	11.080	0.63	2.67
K2O	0.08	0.03	0.07	0.07	0.06	0.13	0.01	0.25	0.28	0.30	0.06	0.14	0.23	0.05	0.12	0.030	0.09	0.22
Total	97.15	100.23	96.96	100.01	97.02	100.04	99.59	96.33	96.40	97.75			97.97	98.17	97.21	102.090	97.93	97.04
Cations (Fe2+/ Fe3+ charge balance)																		
Si	7.488	2.829	7.557	2.833	7.567	2.885	1.970	6.890	6.637	6.557	7.086	6.702	6.934	7.610	6.983	2.933	7.534	6.429
Ti	0.060	0.000	0.053	0.000	0.043	0.001	0.006	0.247	0.296	0.282	0.050	0.042	0.204	0.009	0.041	0.001	0.035	0.326
Cr	0.000	0.000	0.000	0.000	0.000	0.000	0.018	0.000	0.000	0.000	0.039	0.063	0.000	0.000	0.000	0.000	0.000	0.000
Al	0.498	1.173	0.434	1.174	0.436	1.119	0.063	1.352	1.546	1.538	1.134	1.805	1.281	0.523	1.361	1.059	0.608	1.612
Fe3+	0.719	0.000	0.810	0.000	0.732	0.000		0.260	0.306	0.725	1.416	1.303	0.195	0.253	0.338	0.000	0.267	0.990
Fe2+	0.450	0.004	0.277	0.004	0.320	0.004	0.119	1.017	1.149	0.634	0.021	0.031	0.852	1.891	2.276	0.008	1.707	0.780
Mn	0.029	0.001	0.034	0.000	0.026	0.000	0.007	0.030	0.035	0.030	0.000	0.000	0.023	0.037	0.037	0.000	0.033	0.047
Mg	3.756	0.001	3.835	0.000	3.876	0.000	0.858	3.205	3.031	3.233	1.950	1.884	3.511	2.677	1.964	0.001	2.815	2.817
Ca	1.722	0.178	1.660	0.174	1.704	0.134	0.932	1.776	1.806	1.679	0.374	0.596	1.859	1.956	1.904	0.074	1.896	1.546
Na	0.227	0.812	0.204	0.812	0.193	0.849	0.026	0.515	0.617	0.645	0.011	0.026	0.490	0.065	0.422	0.923	0.178	0.755
K	0.014	0.002	0.012	0.004	0.011	0.007	0.000	0.047	0.053	0.055	0.000	0.000	0.042	0.009	0.023	0.002	0.017	0.041
H	2.000		2.000		2.000			2.000	2.000	2.000	0.000	0.000	2.000	2.000	2.000		2.000	2.000
Total	**14.963**	5.000	**14.876**	5.000	**14.908**	5.000	**4.000**	**15.338**	**15.476**	**15.379**	**0.739**	**0.744**	**15.390**	**15.030**	**15.349**	5.000	**15.090**	**15.343**
xMg(Fe2+)	0.89		0.93		0.92		0.88	0.76	0.73	0.84	0.74	0.74	0.80	0.59	0.46		0.62	0.78
Thermometry: T°C																		
Ernst-Liu (K):1998	**599**		**586**		**568**			**866**	**912**	**907**	**578**	**563**	**820**	**498**	**557**		**549**	**941**
Putirka, 2016	*na*		*na*		*na*			**857**	**890**	**907**	*783*	*851*	**860**	*na*	*715*		*na*	**908**
H-B: 1994	**596**		**545**		**548**									**500**	**650**		**565**	*821*
Anorthite		0.18		0.18		0.14										0.07		
Albite		0.82		0.82		0.86										0.93		
Orthoclase		0.00		0.00		0.01										0.00		

facies conditions. Then, a single brown amphibole gradually changes to a green hornblende (gHbl) and corresponds to an amphibolite facies stage. The green hornblende is finally progressively replaced by actinolite with associated chlorite and epidote (Act+Chl + Ep) corresponding to the greenschist facies.

In this sample, a millimeter wide shear zone is identified and contains a string of titanite +/−ilmenite, monazite and xenotime grains surrounded by green amphibole and plagioclase (Fig. 8). Mineral textures reveal three titanite populations in this rock: (1) titanite associated with the green coronitic amphibole (Fig. 6) (2) titanite associated with other accessory minerals in the tiny ductile shear zone (Figs. 8) and (3) titanite recrystallised with rutile, after ilmenite (Fig. 9).

Sample CH5: Metatroctolites are abundant on the few tens of meters at the base of the massif. The ferromagnesian minerals are largely dominant over the plagioclase. Another notable outcrop from which the sample CH5 (Fig. 10) was collected is located on the middle of the SW ridge of the Mont Chenaillet. In all these rocks, olivine is always absent and is replaced, at the contact with plagioclase by a coronitic aggregate composed of amphibole (tremolite) enclosed by a chlorite rim. Rare clinopyroxene, brown and/or green hornblendes and oxides can also be found.

4. Analytical techniques

4.1. Electron probe microanalysis (EPMA)

Titanite and monazite were analysed for major and minor elements with an EPMA CAMECA SX100 at Laboratoire Magmas et Volcans (LMV). For titanite, analyses were made with an accelerating voltage of 20 kV and a 40 nA beam current. The crystals used for analysis were PET for Ca, Ce and S, TAP for Si, Na and Y, LPET for P, Cl, La and Sr, and PC0 for F and O. For monazite, analyses were made accelerating voltage of 15 kV and a 40 nA beam current. The crystals used for analysis were PET for Ca, Si, La, Th, U and Ce, LPET for P, Y and Pb, and LLIF for Pr, Nd, Sm and Gd. Several trace elements in these minerals were also analysed for comparison with laser ablation ICP-MS (LA-ICPMS) data or when these minerals where too small. The different mineral studied in this contribution were imaged for back-scattered electrons (BSE) using this microprobe.

4.2. Laser ablation-inductively coupled plasma mass spectrometry (LA-ICP-MS)

4.2.1. Trace element analyses

Trace element analysis of titanite was done by laser ablation-inductively coupled plasma mass spectrometry (LA-ICP-MS) using a

Metagabbro Ch3														**Albitite - CH4**		
6					**5**											
Pl	BHbl	BHbl	LbHblCor	PlCor	LbHblCor	LbHblCor	LbHblCor	LbHblCor	BHbl	BHbl	BHbl	BHbl	BHbl	Hbl	Hbl	PL
65.15	44.46	44.37	45.91	66.09	47.59	45.82	46.55	46.51	44.88	44.54	44.54	44.90	44.83	46.09	47.89	67.88
0.00	2.76	3.00	1.49	0.03	1.38	1.73	1.62	1.51	3.02	3.07	2.82	2.97	3.06	1.50	1.63	0.00
0.00				0.00												0.03
21.78	9.13	8.62	8.15	21.38	6.58	7.47	7.35	7.06	8.57	8.73	8.66	8.51	8.51	6.79	6.72	20.76
0.11	14.66	15.67	15.49	0.11	15.45	15.68	15.63	15.42	16.05	15.71	15.69	16.06	15.67	17.22	17.28	0.20
0.00	0.49	0.54	0.52	0.02	0.52	0.51	0.55	0.48	0.55	0.60	0.58	0.59	0.56	0.59	0.65	0.01
0.00	13.15	12.65	13.11	0.00	13.69	12.76	13.35	13.53	12.45	12.49	12.42	12.10	12.25	12.75	13.00	0.01
2.85	9.81	9.55	9.97	2.07	10.21	10.03	9.94	9.77	9.43	9.36	9.71	9.73	9.58	9.27	9.04	1.17
9.73	2.66	2.60	2.08	10.53	1.85	2.03	2.02	2.07	2.62	2.64	2.52	2.64	2.51	2.22	2.30	10.20
0.17	0.21	0.20	0.19	0.02	0.21	0.18	0.22	0.15	0.21	0.21	0.29	0.22	0.17	0.32	0.28	0.17
99.78	97.33	97.22	96.92	100.24	97.49	96.22	97.25	96.59	97.78	97.36	97.28	97.73	97.15	96.79	98.80	100.43
2.882	6.453	6.466	6.663	2.897	6.863	6.732	6.734	6.761	6.505	6.47679	6.50652	6.54904	6.54840	6.72291	6.81056	2.982
0.000	0.301	0.329	0.163	0.001	0.150	0.191	0.176	0.165	0.329	0.33568	0.30976	0.32574	0.33610	0.16452	0.17430	0.000
0.000	0.000	0.000	0.000	0.000	0.000	0.000	0.000	0.000	0.000	0.00000	0.00000	0.00000	0.00000	0.00000	0.00000	0.001
1.135	1.562	1.481	1.394	1.105	1.118	1.294	1.253	1.210	1.464	1.49637	1.49119	1.46311	1.46525	1.16744	1.12648	1.075
0.000	1.092	1.175	1.233	0.000	1.146	1.092	1.238	1.285	1.165	1.17915	1.06926	0.95904	1.02493	1.47315	1.46429	0.000
0.004	0.687	0.735	0.647	0.004	0.717	0.834	0.653	0.589	0.780	0.73110	0.84731	0.99971	0.88906	0.62718	0.59059	0.007
0.000	0.060	0.067	0.064	0.001	0.064	0.063	0.067	0.059	0.068	0.07390	0.07176	0.07289	0.06928	0.07289	0.07829	0.000
0.000	2.845	2.748	2.836	0.000	2.942	2.794	2.878	2.931	2.689	2.70701	2.70419	2.63047	2.66698	2.77190	2.75549	0.001
0.135	1.525	1.491	1.550	0.097	1.577	1.579	1.541	1.521	1.464	1.45817	1.51964	1.52043	1.49918	1.44861	1.37730	0.055
0.834	0.748	0.735	0.585	0.895	0.517	0.578	0.566	0.583	0.736	0.74423	0.71366	0.74650	0.71078	0.62777	0.63410	0.869
0.010	0.039	0.037	0.035	0.001	0.039	0.034	0.041	0.028	0.039	0.03895	0.05404	0.04093	0.03168	0.05954	0.05079	0.010
	2.000	2.000	2.000		2.000	2.000	2.000	2.000	2.000	2.00000	2.00000	2.00000	2.00000	2.00000	2.00000	
5.000	**15.313**	**15.263**	**15.171**	5.000	**15.133**	**15.191**	**15.148**	**15.133**	**15.239**	**15.24135**	**15.28734**	**15.30786**	**15.24164**	**15.13592**	**15.06220**	5.00000
	0.81	0.79	0.81		0.80	0.77	0.82	0.83	0.78	0.79	0.76	0.72	0.75	0.82	0.82	
	922	**944**	**761**		**743**	**796**	**780**	**764**	**946**	**950**	**927**	**941**	**949**	**762**	**782**	
	900	**892**	*836*		*806*	*828*	*827*	*825*	**885**	**892**	**882**	**879**	**881**	**817**	**812**	
			758		**727**	**750**	**746**	**742**	*790*	*794*	*790*	*787*	*786*	*735*	*721*	
0.14				0.10												0.06
0.85				0.90												0.93
0.01				0.00												0.01

Thermo Element XR coupled to a 193 nm excimer laser (Resonetics Resolution M-50E) at LMV. The spot size was 20 μm with a repetition rate of 1 Hz and a fluence of 3 J/cm^2. We purposely set a low frequency to avoid drilling through titanite too quickly. Each run lasted 20 s of background acquisition plus 90s of analyses. Each sequence was bracketed by two analyses of GSE-1G or GSD-1G standards at the beginning and at the end of the sequence (Jochum et al., 2005). Khan titanite reference material (Heaman, 2009) was regularly analysed throughout the analytical session to monitor data quality at the same spot size as the analysed unknowns to account for downhole fractionation. Hf content was monitored during analysis of titanite in order to identify potential micro inclusions of zircon. All analyses with Hf content above the background values were discarded. Internal normalisation for LA-ICP-MS data was done using ^{43}Ca and data processing was conducted using the GLITTER software (Griffin, 2008).

4.2.2. U—Pb dating

Zircon, monazite, titanite and xenotime have been analysed in thin section by LA-ICP-MS (Laboratoire Magmas et Volcans, Clermont-Ferrand, France) in order to control the position of the grain relative to the textures observed in the sample. These minerals were ablated under pure He using a Resonetics Resolution M-50 system equipped with a 193 nm Excimer laser coupled to a Thermo Element XR sector field ICP-MS using a jet interface high-capacity pumping device for zircon and titanite or an Agilent 7500 cs quadrupole ICP-MS equipped with a dual pumping system for monazite and xenotime. N_2 was supplemented to Ar and He carrier gas for sensitivity enhancement (Paquette et al., 2014). The laser operated with a spot diameter of 27 μm, a repetition rate of 3 Hz, and a fluence of 2.5 J/cm^2 for zircon and titanite and a spot diameter of 9 μm, a repetition rate of 1 Hz, and a fluence of 4.0 J/cm^2 for monazite and xenotime, respectively.

The instruments were tuned to maximise the ^{238}U intensity and minimise ThO$^+$/Th$^+$ (<1%) using the NIST SRM 612 glass. Background levels were measured on-peak with the laser off for ~30 s, followed by ~60 s of measurement with the laser firing and then ~10 s of washout time (Hurai et al., 2010). Reduction of raw data was carried out using the GLITTER® software package (van Achterbergh et al., 2001). Isotope ratios were corrected for laser-induced and instrumental mass fractionation via sample-standard bracketing using the GJ-1 zircon reference material (Jackson et al., 2004) for zircon and titanite (Fallourd et al., 2014) and the Trebilcock monazite reference material (Tomascak et al., 1996) for monazite and xenotime, respectively. The ^{235}U signal is calculated from ^{238}U based on the ratio ^{238}U/^{235}U = 137.818 (Hiess et al., 2012). The 91,500 zircon reference material (Wiedenbeck et al., 1995) and the Itambe and Bananeira monazites (Gonçalves et al., 2016) were analysed along with the samples to independently monitor the

Fig. 4. Metagabbro (CH3), a few meters from the gabbro-serpentinite contact (on the top of the gabbro outcrop of the Fig. 2). Gray pyroxenes and black amphiboles, both magmatic, are wrapped in a foliation, which is underlined by a black amphibole. Abbreviations in text and figures are from Whitney and Evans (2010)

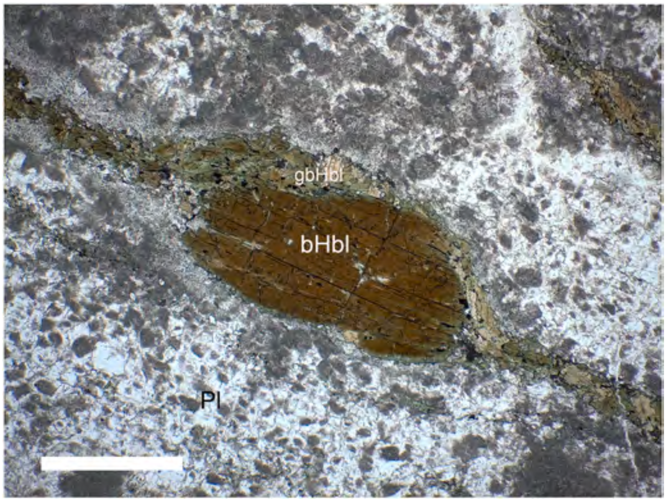

Fig. 5. Coronitic amphibole in the metagabbro CH3: the porphyclast of brown amphibole is wrapped by foliation and surrounded by green-brown amphibole and ilmenite, testifying to a ductile high temperature deformation and metamorphism during cooling of the gabbro. Microphotography in Plane Polarized Light; white bar: 1 mm. (For interpretation of the references to colour in this figure legend, the reader is referred to the web version of this article.)

external precision and accuracy of the measurements. Common Pb was not corrected owing to the large isobaric interference of ^{204}Hg. Concentrations of U, Th, and Pb were calculated by normalisation to the certified composition of GJ-1 reference material. ^{207}Pb/^{206}Pb versus ^{238}U/^{206}Pb diagrams (Tera and Wasserburg, 1972) were generated using Isoplot/Ex v. 2.49 software package by Ludwig (2001). Error ellipses for each point are quoted at the 2σ level.

5. Results

5.1. Mineral chemistry and geothermometry

The metamorphic minerals are brown to green amphiboles and actinolite, epidote, albite – oligoclase, chlorite, ilmenite, titanite and titanite-rutile (after ilmenite). In the classification for calcium amphiboles by Leake et al. (1997), amphiboles ranged as magnesio-hornblendes and actinolites (Table 1). The colour of the amphibole, brown to green, depends on the titanium content of the mineral. Primary brown hornblende of sample CH3 is rich in titanium and range in composition between 2.5 and 3 wt% TiO_2. On the other hand, coronitic light brown hornblende TiO_2 content is around 1.50 wt% while below 0.40 wt% for green amphibole. The concentrations of brown and green hornblende located in coronas of CH1 metagabbto are 2.66–1.90 wt% and around 0.40 wt% respectively. In this sample, green actinolite of the tiny shear zone which contains the string of titanite +/−ilmenite, monazite and xenotime has similar low values TiO_2 (≈ 0.40 wt%). Finally, in CH4 sample, TiO_2 concentrations in the green hornblendes of the albititic vein are 1.50–1.60 wt%. Brown hornblendes, light brown hornblendes, green hornblendes, actinolite are progressively less and less rich in this element. Overall, the composition of plagioclase is very acidic in all rocks: it ranges from albite to oligoclase (Table 1).

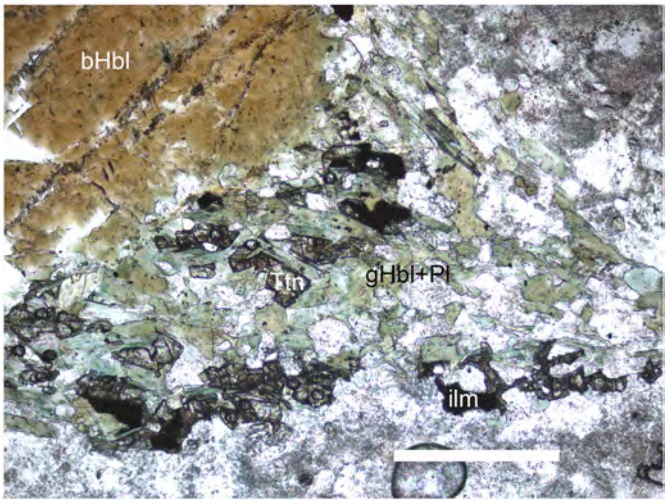

Fig. 6. Coronitic assemblage in the metagabbro CH3: microphotography of a pressure shadow of green amphibole (gHbl) – plagioclase – titanite (Ttn) +/−ilmenite (ilm, itself replaced by titanite + rutile as in Fig. 9) around a brown amphibole (bHbl) (Microphotography in PPL); white bar: 0,25 mm. (For interpretation of the references to colour in this figure legend, the reader is referred to the web version of this article.)

Provided that a titaniferous buffer mineral as titanite, ilmenite or rutile is present, the change from brown to green amphibole reflects a decrease in the concentration of this element and of the temperature. The concentration of Ti is temperature-dependent and can be used as a robust geothermometer (Otten, 1984; Ernst and Liu, 1998; see below). In a first approach, the brown to green colors of the hornblendes are good qualitative thermometric indicators and reflect respectively high to low temperature conditions of the granulite and amphibolite facies; actinolite is evidence of greenschist facies conditions.

Temperature estimates were acquired by applying amphibole-based geothermometers. We used the hornblende–plagioclase geothermometer of Holland and Blundy (1994; Jaffrey et al. (1971) edenite-tremolite calibration) and the amphibole-only thermobarometers by Ernst and Liu (1998) and Putirka (2016). We previously noted that the mineralogical assemblages in a single rock are not always in equilibrium and record different stages of the thermal history of the massif. Accordingly, the hornblende-plagioclase geothermometer must be used with caution and the equilibrium between the mineral pairs must be carefully checked. On the other hand, geothermometers only based on the amphibole composition do not have this drawback. The semi-quantitative amphibole thermobarometer of Ernst and Liu (1998) is based on Ti content of the M2 site that increases with temperature. The use of Ti thermometer requires an excess of Ti in the system: we assume that this condition is satisfied because ilmenite and/or titanite

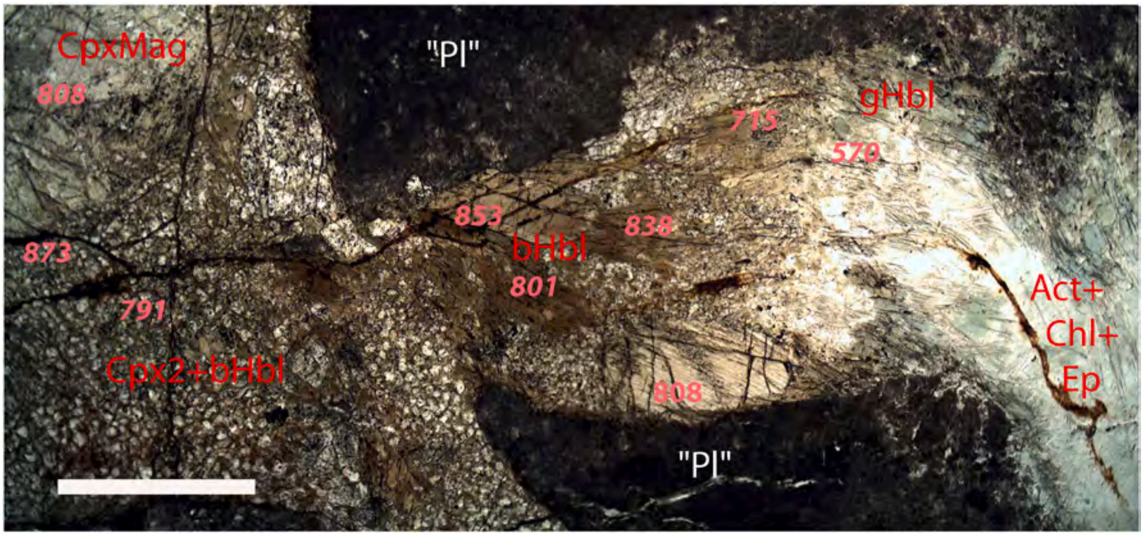

Fig. 7. Complex coronitic assemblage in the metagabbro CH1: From left to the right, i.e. from the magmatic clinopyroxene clasts to plagioclase: the magmatic clinopyroxene clasts (CpxMag) are recrystallised into a fine granoblastic aggregate of Cpx2 wrapped with interstitial brown hornblende (Hbb) (=granulite facies). Then, a single brown amphibole gradually changes to a green hornblende (GHbl) (= amphibolite facies), then to an actinolite associated with chlorite and epidote. (Act+Chl + Ep) (= greenschists facies). The plagioclase ("Pl") is black with a dusty aspect: it is replaced by a fine aggregate of epidote and albite (= prehnite - pumpellyite facies). Temperatures in °C according to the Ti-amphibole thermometer of Ernst and Liu *(1998, « revisited »)*. This portion of rock records on only 3 mm, the cooling of the gabbro through the Granulite, Amphibolite and Greenschists facies. (Microphotography in PPL)*;* white bar: 1 mm. (For interpretation of the references to colour in this figure legend, the reader is referred to the web version of this article.)

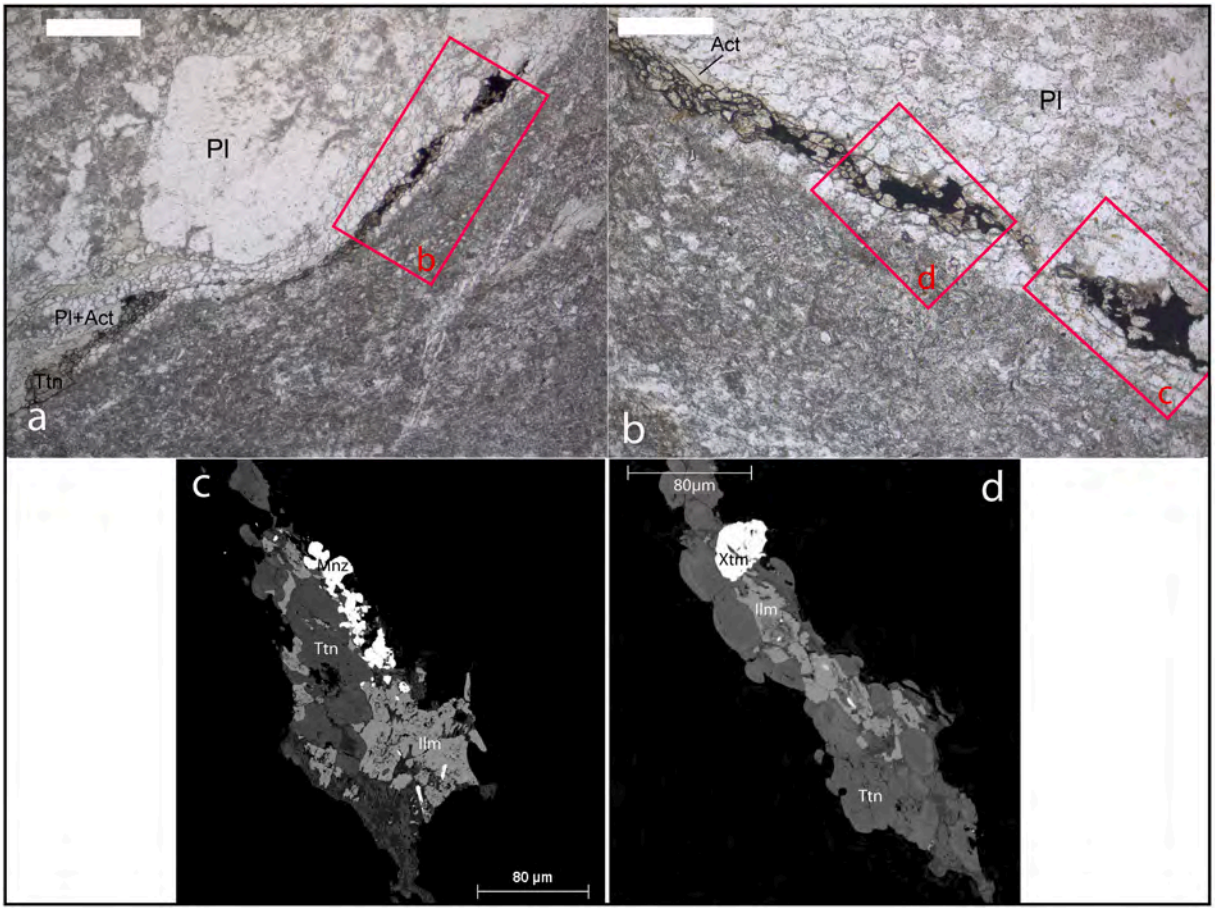

Fig. 8. A string of chronometer minerals in sample CH1: a string of titanite +/− ilmenite grains is located in an amphibolitic layer with a granoblastic texture. a) and b) microphotographs in PPL. In white in c) and d) respectively xenotime and monazite in the string; titanite is dark gray, ilmenite is light gray. Backscattered electron (BSE) images; *w*hite bar: 0.4 mm in a); 0.2 mm in b).

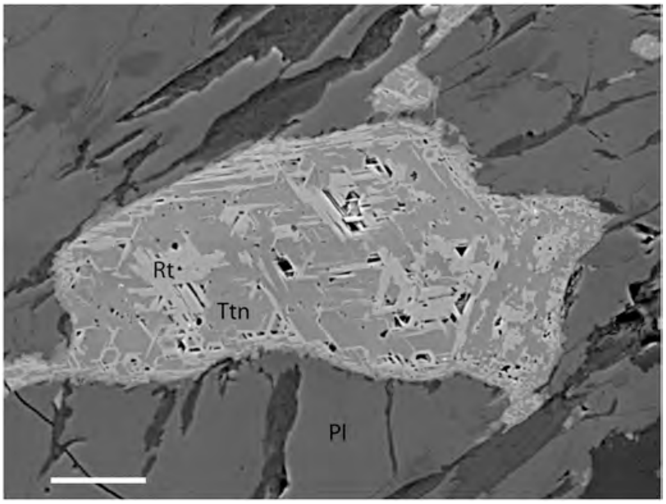

Fig. 9. Destabilization of ilmenite into titanite + rutile needles. Backscattered electron (BSE) image.*)*; sample CH1; white bar: 20 μm.

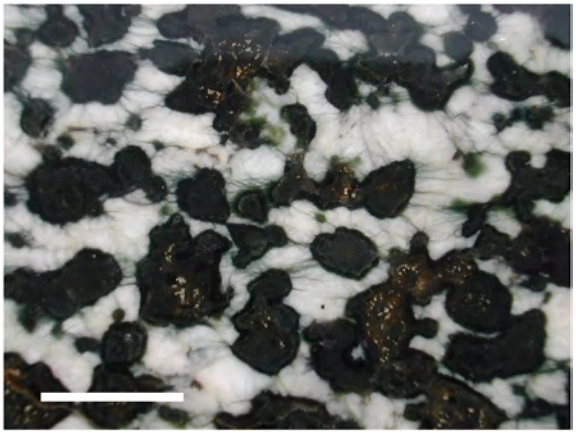

Fig. 10. Photography of a metatroctolite: at the contact with plagioclase, olivine is replaced by a coronitic aggregate, composed of an amphibole (tremolite) enclosed by a chlorite rim according to the reaction Ol + Pl + V = chlorite + tremolite. White bar: 1 cm.

are always present. The accuracy of this thermometer has been estimated at the Institut für Mineralogie of Hannover (Germany) using published and unpublished experimental data (J. Koepke, pers. Comm.). The equation of this geothermometer is given in France et al. (2021). For the amphibole-only thermobarometer of Putirka (2016), we used eq. 6 with a lithostatic pressure of 0.2 Gpa, which is compatible with the depth of gabbro emplacement in a crust formed at slow spreading ridges (e.g. Canales et al., 2017). In any case, eq. 6 of the Putirka thermometer is almost insensitive to small pressure changes (2.4 °C/0.1 GPa). It has to be noted that, the amphibole-only thermobarometer of Putirka, (2016) was calibrated for igneous systems with $T > 650$ °C and therefore is preferably suitable for estimating temperature conditions from igneous and high-grade metamorphic rocks (Molina et al., 2021).

Temperatures obtained for the two samples CH1 and CH3 with both amphibole-only thermometers for brown amphiboles are consistent and vary between 950 °C and 850 °C (Table 1). On the other hand, the hornblende-plagioclase geothermometer using brown amphibole gives lower results (790–820 °C, Table 1). This discrepancy between the amphibole-only and the hornblende–plagioclase geothermometers can be explained by the fact that plagioclase of acidic composition is no longer in equilibrium with high temperature Ti-rich amphiboles. In general, the temperatures recorded by all geothermometers using green amphiboles are lower (between 800 °C and 550 °C; Table 1). For the entire range of green hornblende compositions, Ti-in amphibole thermobarometer of Ernst and Liu (1998; « revisited » by Koepke) and the hornblende-plagioclase geothermometer give equivalent results. However, the Purtika's amphibole-only thermometer (2016) tends to give higher estimates and overestimates the temperatures of amphibolite and greenschist facies conditions Consequently, we did not apply it to the amphiboles of the greenschist facies.

In the CH3 sample, oikocrysts of Ti-rich amphibole indicate temperatures between 880 °C–910 °C (therm. Purtika) and 950 °C (therm. Ernst and Liu, 1998 « revisited ») (brown amphiboles in Figs. 5 and 6; Table 1). Their formation occurs at a late-magmatic stage prior to retrograde metamorphism. The light brown coronitic amphibole, located around the brown primary amphibole and contemporary to the ductile deformation, indicates temperatures around 800–750 °C(therm. Ernst and Liu, 1998 « revisited »), 800–830 (therm. Purtika) and 730–750 °C (therm. Holland and Blundy; Fig. 5 and Table 1). This highlights that deformation immediately followed the emplacement and the crystallisation of the gabbro. The light-brown- to green amphibole coronas record decreasing temperatures from 800 °C (Fig. 5) down to 550 °C (Fig. 6).

In the remarkable assemblage around the clinopyroxene of the CH1 sample, temperatures range from 870 °C to 570 °C (Fig. 7). In the amphibolitic layer containing the string of titanite, monazite, ilmenite and xenotime (Fig. 8), we note the consistency of the temperatures obtained with hornblende –plagioclase geothermometer (550–600 °C) and those acquired with the Ti-amphibole thermobarometer of Ernst and Liu (1998) (550–600 °C). These are the temperatures of the amphibolite-greenschist transition around 550–600 °C as attested by the actinolite + plagioclase paragenesis.

According to the amphibole geothermometry, the crystallisation temperature of the albitite vein is around 760 and 780 °C (therm. Ernst and Liu, 1998 « revisited »), 815 °C (therm. Purtika; Table 1).

5.2. *Trace elements in titanite*

In CH1, three types of titanite in different textural context were analysed: (1) titanite cristallising in the green hornblende corona at the expanse of the Ti-rich brown amphibole, (2) titanite crystallising at the expense of ilmenite (Figs. 9) and (3) titanite associated with the string of accessory minerals in a tiny ductile shear zone (Fig. 8). In Fig. 11a, a diagram reporting Y vs. Nb reveals that these three types of titanite are chemically different. Types 1 and 2 have lower Nb and Y contents ($145 < \text{Nb} < 1982$ ppm and $80 < \text{Y} < 18{,}328$ ppm, respectively), while type 3 has high Nb and Y contents ($2764 < \text{Nb} < 5158$ ppm and $19{,}163 < \text{Y} < 29{,}017$ ppm, respectively). Type 3 has overall much-richer trace elements content than types 1 and 2 (Table 2 and supplementary data_2). In CH3, titanite located within the green amphibole corona (type 1) have the same chemical characteristics as for CH1 sample (Table 2 and supplementary 2). In CH3, another type of titanite (type 4) occurs in late fractures. Although most trace elements in type 4 have fairly similar content to types 1–2 (Table 2 and supplementary data_2), it has generally higher Nb, Cr, V and Sn contents (77–250 ppm, 47-118 ppm, 353–594 ppm and 35–97 ppm) than type 1 titanite (24–111 ppm, 9–97 ppm, 247–480 ppm and 15–35 ppm respectively).

Chondrite-normalized REE patterns (Fig. 11b) also distinguish the different types of titanites described above: type 1 titanites from CH3 sample have low REE content, rather flat patterns and moderate positive to negative Eu anomalies. In contrast, type 3 from CH1 sample corresponding to titanite from the accessory mineral of the ductile shear (Fig. 8), define a tight group 20–200 times richer in REE content, with quite flat REE patterns and a strong negative Eu anomaly (Fig. 11b, Table 2 and supplementary data_2). Notably, type 3 titanite define a tight group of analyses in a Chondrite-normalized diagram while the other titanite types analyses are more scattered. Finally type 4 titanites

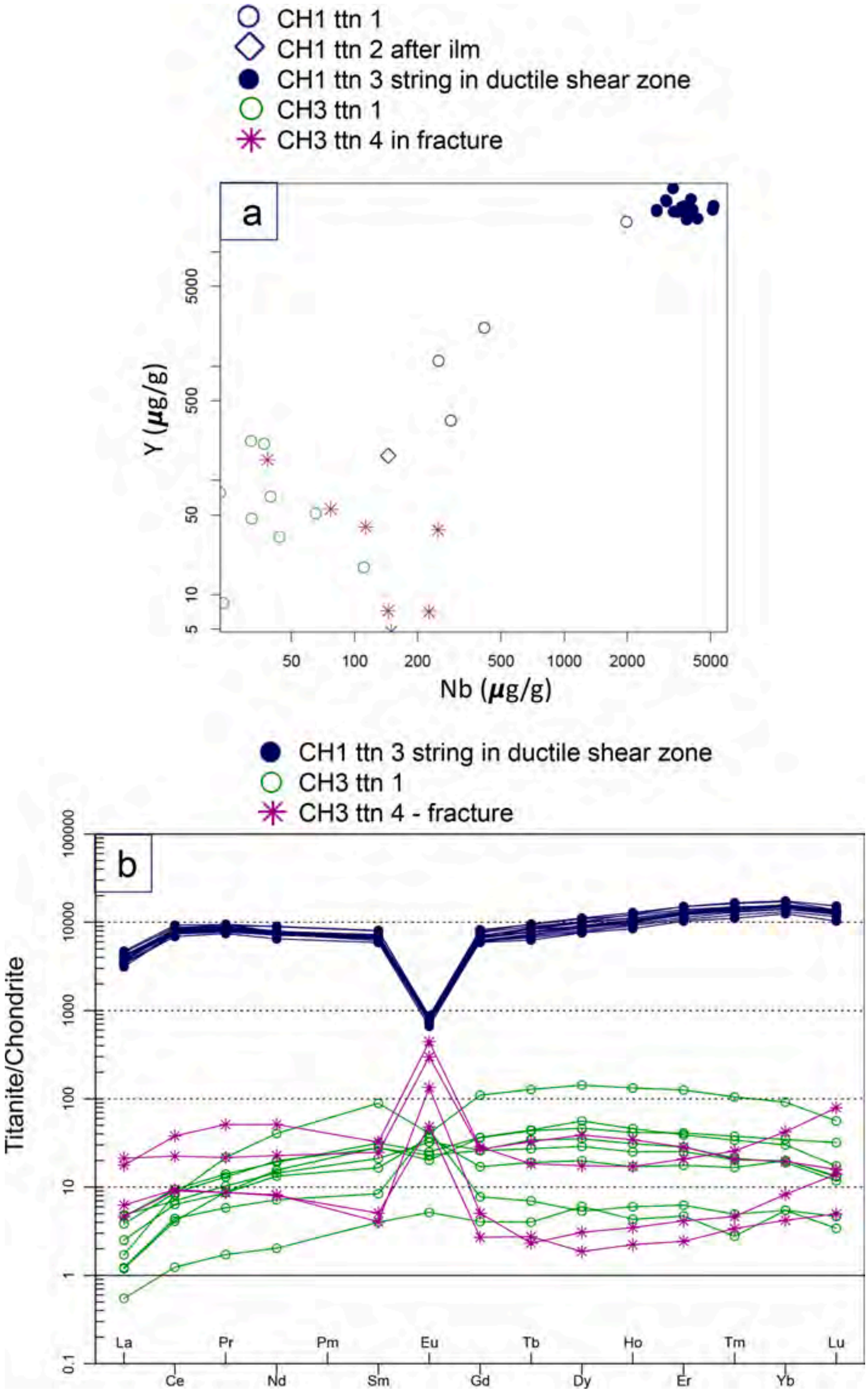

Fig. 11. (a): Y vs Nb in ppm, (b) Chondrite-normalized REE patterns of the titanites of the metagabbros CH1 and CH3. Chondrite values from Boynton (1984).

from sample CH3 display similar REE patterns to those of type 1 from the same sample but with a marked positive Eu anomaly. Type 4 titanite texturally occurs in late fractures and Eu anomaly in this titanite type is most probably inherited from late fluid circulation and local feldspar alteration.

5.3. U-Th-Pb geochronology

5.3.1. Ages of the magmatism recorded by zircon

The zircons from the CH1 gabbro and the CH4 albitite vein allow dating the crystallisation and the emplacement of the massif. The zircon crystals of the gabbro CH1 are 30–100 µm long, subhedral and sometimes cracked. Cathodoluminescence images (Fig. 12a) show oscillatory zoning: such internal structure is well consistent with those of zircons crystallised from mafic magmas (Corfu et al., 2003; Paquette et al., 2017). In the metagabbro, U and Th contents are very variable, from 9 to 342 ppm and from 2 to 130 ppm, respectively, whereas the Th/U ratios also yield magmatic values, ranging from 0.10 to 0.49. Reported in a Tera-Wasserburg diagram, thirty-four of the thirty-five analysed points plot on a discordia line which allows to calculate a lower intercept age of

Table 2

Representative analyses of titanite: major and trace elements: Electron microprobe and LA-ICP-MS analyses.

Sple	CH1 sample										CH3 sample				
Micr.	ttn string			ttn from matrix			ttn in ghb corona			ttn after ilm	ttn in ghb corona		ttn from late fracture		
(wt%)	2	3	4	20	21	22	23	24	25	26	28	32	43	44	49
SiO2	28.63	28.88	28.60	31.61	31.09	28.99	30.77	30.79	31.23	30.72	30.99	30.73	30.91	30.74	30.93
Al2O3	1.44	1.34	1.66	4.19	2.81	1.38	1.60	1.39	3.02	0.77	1.56	2.35	1.14	1.40	2.24
F	0.12	0.01	0.07	0.28	0.08	0.05	0.09	0.10	0.13	0.12	0.04	0.15	0.09	0.12	0.11
CaO	24.61	24.81	24.50	28.03	27.98	25.47	28.38	28.42	28.58	28.36	28.65	28.73	28.63	28.96	28.97
TiO2	34.89	34.83	34.62	32.45	35.62	35.23	37.22	37.84	35.38	39.00	38.37	36.62	38.44	38.33	36.94
La2O3	0.15	0.16	0.17	0.02	bdl	0.17	0.01	bdl	bdl	bdl	bdl	bdl	bdl	0.02	bdl
Nb2O5	0.61	0.74	0.43	0.04	0.06	0.28	0.00	0.04	0.00	0.02	0.02	bdl	0.02	0.01	bdl
ZrO2	0.05	0.07	0.04	bdl	0.03	0.05	0.13	0.06	0.01	bdl	0.02	bdl	0.01	0.03	bdl
P2O5	0.06	0.08	0.04	0.01	0.00	0.06	0.01	0.03	0.01	bdl	0.07	0.10	0.03	0.01	0.01
Y2O3	3.16	2.68	3.49	0.04	0.28	2.33	0.04	0.14	0.01	0.02	0.01	bdl	bdl	0.02	bdl
FeO	1.73	1.67	1.86	1.17	0.56	1.57	0.78	0.45	0.71	0.42	0.53	0.83	0.80	0.59	0.70
MnO	0.07	0.06	0.05	0.03	0.02	0.06	0.00	0.02	0.01	bdl	bdl	0.04	0.03	0.01	0.02
Ta2O5	0.36	0.45	0.27	bdl	bdl	0.03	bdl	bdl	bdl	0.02	0.01	0.02	bdl	bdl	bdl
Cr2O3	bdl	bdl	bdl	0.00	bdl	0.46	0.05	0.16	0.02	0.01					
LA-ICPMS data (ppm)															
La	1258	1402	1048	130*		1416*	125*				0.2	0.8	1.4	5.5	6.6
Ce	6353	7088	5562								1	5.1	7.3	30.7	18.1
Pr	1041	1085	909								0.2	1.1	1.1	6.2	2.6
Nd	4537	4799	3896								1.2	8.0	4.9	30.7	13.7
Sm	1306	1270	1149								0.8	3.2	0.8	6.3	4.8
Eu	57	61	49								0.4	2.7	9.9	32.6	21.9
Gd	1709	1575	1588								1.1	4.4	1.3	7.4	6.9
Tb	364	317	343								0.2	0.9	0.1	0.9	1.6
Dy	2787	2502	2767								1.9	6.4	1.0	5.6	12.5
Ho	738	657	714								0.3	1.2	0.3	1.2	2.5
Er	2586	2248	2534								1.0	3.7	0.9	4.4	5.9
Tm	465	391	432								0.1	0.5	0.2	0.8	0.7
Yb	3291	2758	2961								1.1	4.2	1.7	8.9	4.1
Lu	428	373	402								0.1	0.4	0.5	2.6	0.5
Sc	11	9	10								bdl	bdl	1.8	2.3	7.0
V	588	553	591								247	463	594	549	363
Cr	608	568	986								9.1	48.8	74.1	117.3	54.5
Sr	20	20	19								15.4	30.6	39.3	47.8	276.2
Y	23,416	19,557	22,521	335*	2170*	18,328*	304*	1116*	83*	165*	8.5	32.2	7.2	36.9	56.2
Zr	571	539	449		194*	362*	998*	417*	57*		95.3	26.1	59.8	267.7	42.6
Nb	4101	4321	3326	288*	416*	1982*		252*		145*	23.7	43.9	144.6	250.3	77.1
Mo	47	54	37								0.7	5.3	3.0	2.1	2.8
Sn	274	274	220								11.7	19.4	96.3	83.4	35.1
Sb	bdl	bdl	bdl								bdl	bdl	bdl	bdl	bdl
Hf	104	91	81								2.7	1.0	2.5	9.3	1.9
Ta	3153	3405	2132			262*				120*	0.4	1.4	0.7	5.1	0.8
W	4	4	3								bdl	2.3	0.4	0.4	0.1
Pb	3	3	2								0.1	0.3	0.1	0.1	2.4
Th	176	162	136								0.0	0.0	0.1	0.6	0.1
U	163	164	154								0.0	0.1	0.5	4.6	0.6

bdl = below detection limit.

* calculated from microprobe data.

161.0 +/− 0.8 Ma (Fig. 12a).

In the albitite vein (CH4), several crystals form rectangular half-millimeter tablets with square or diamond-shaped cross-sections. Slight localised alteration along fractures is noticeable in cathodoluminescence (Fig. 12b). However, the network of these fractures is sufficiently spaced to allow analyses by laser-ICPMS. The U and Th contents of zircons from CH4 are very low, from 8 to 31 ppm and from 2.8 to 19.5 ppm, respectively, in agreement with a mantle-derived source. The Th/U ratios ranging from 0.36 to 0.65 display typically magmatic values (Table 3). Reported in a Tera-Wasserburg diagrams, the seventeen analytical points define a discordia line which yields a lower intercept at 161.8 +/− 1.7 Ma (Fig. 12b).

Both dates, 161.8 +/− 1.7 Ma and 161.0 +/− 0.8 Ma, attest of the age of the emplacement of the gabbroic massif and associated rocks.

5.3.2. *Ages of the cooling recorded by the metamorphic chronometer minerals: monazite, xenotime and titanite*

All three metamorphic chronometer minerals, monazite, titanite and xenotime are found in a tiny shear zone in sample CH1.They date this shearing event which occurs during the cooling of the gabbro when this one reached the greenschist facies conditions. A cluster of a few rounded grains (around ten) of monazites ranging in size from 5 to 20 μm is associated with the string of titanite and ilmenite. (Fig. 8c). Composition of monazite is relatively homogeneous. UO_2 contents are low and vary between0.15 and 0.42%, while ThO_2 varies from 1.36 to 5.06% (Table 3).

Four small grains of xenotime are included in the string. Only a single grain of 50 × 30 microns size could be analysed for dating. (Fig. 8d).

We noted previously that three populations of titanite can be distinguished by their petrographic textures and their compositions in the sample CH1 (Table 2 and supplementary data_2). Crystals associated with green Hbl + Pl coronas around Cpx/brown hornblende and rare

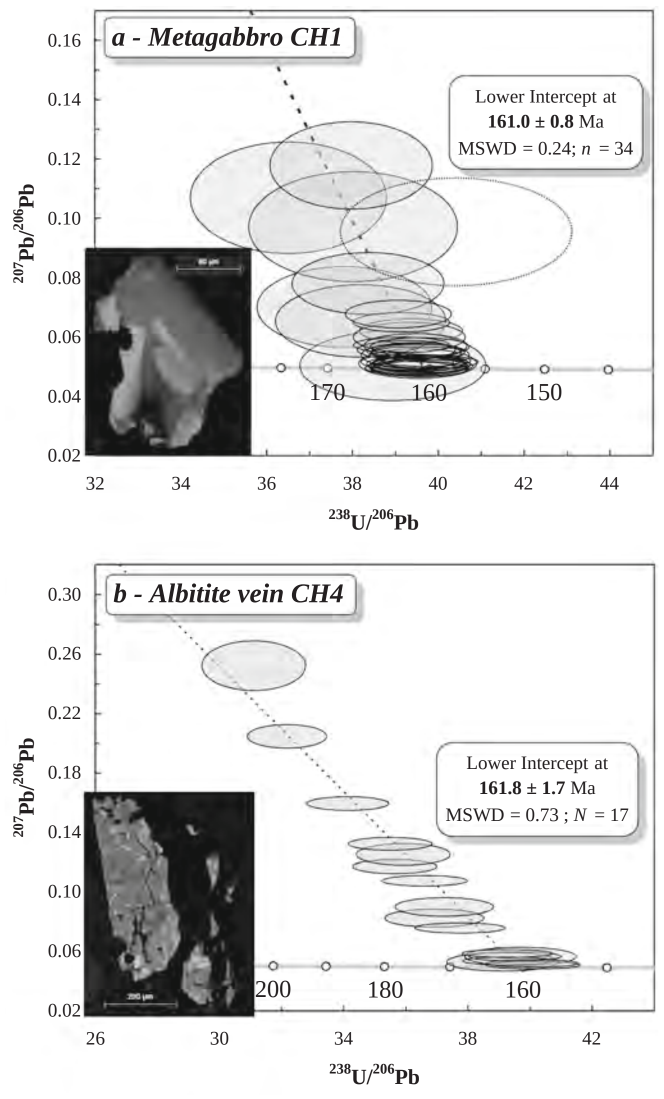

Fig. 12. Geochronological results: Tera–Wasserburg diagram showing the zircon data of (a) the gabbro CH1 and (b) the albitite vein CH4. Cathodoluminescence images of zircons. In a), note the oscillatory zoning; in b), a slight alteration is localised at the fractures; the size of the analysis spot (30 μm) is smaller than the size of the fracture network.

crystals scattered in the rock are poor in trace elements (Fig. 6). Those included in the string of titanite +/− ilmenite associated to monazite and xenotime grains and located in a millimetric amphibolitic layer (Fig. 8) are rich in trace elements (Table 2 and Fig. 11). Their fairly high Th and U contents (up to 222 ppm and 187 ppm respectively) allow dating of these minerals.

The analytical points of the U—Pb dating of the three minerals: monazite, xenotime and titanite plot along discordia lines and yield lower intercept ages at 161.3 ±4.0 Ma, 161.5 ±2.4 Ma and 158.4±2.3 Ma, respectively (Fig. 13). These three ages are consistent within the analytical uncertainties.

6. Discussion: retrograde evolution of the (meta)gabbro of Mont Chenaillet - dating and modelling the cooling

6.1. Metamorphism and cooling of the gabbro

In the Mont Chenaillet massif, isotropic gabbros, foliated metagabbros and amphibolites coexist, showing that deformation and metamorphism are unevenly distributed. The petrographic relationships in the studied rocks show a chronology in the crystallisation of the amphiboles, gradually passing from brown to green, then to actinolite, this evolution being documented in the Fig. 7. The mineral assemblages are consistent with peritectic reaction as clinopyroxene + melt + fluid → amphibole + plagioclase and the hydrothermal metamorphic reactions: clinopyroxene + calcic plagioclase + fluid → amphibole (+ clinopyroxene 2) + sodic plagioclase and dark brown-amph + An-rich Pl1 = light brown amph /green amph + Ab rich Pl2 + ilmenite/titanite. In metatroctolite outcrops, the absence of olivine supposes the involvement of the reaction olivine + plagioclase + fluid = tremolite + chlorite (Fig. 10). These amphibole-forming reactions were continuously retrogressive and they testify that the different rocks record the cooling history of the massif. These minerals are, however, unevenly distributed throughout the whole massif. This requires a pervasive and continuous infiltration of aqueous fluids/hydrated melt over time but which are more or less channelised.

In this contribution, we aimed at dating different minerals testifying of the magmatic (zircon) and cooling history (monazite, titanite, xenotime). The dates recorded in the zircon, 161.8 +/− 1.7 Ma and 161.0 +/− 0.8 Ma, constrain the age of the emplacement of the gabbroic massif and associated rocks. They are similar within uncertainties with those published in Li et al. (2013). They are consistent with the ages of the oceanic sediments of the Lago Nero-Replatte unit, the neighbouring ophiolite body which contains radiolarites providing a middle bathonian age between 166 and 162 Ma. (Cordey and Bailly, 2007). On the other hand, the three metamorphic minerals, monazite, titanite and xenotime (belonging to the greenschist paragenesis of the tiny shear zone of sample CH1) crystallised between 550 and 600 °C and thus date the transition from amphibolite facies to greenschist facies during the cooling of the gabbro. The three ages obtained: 161.3 ±4.0 Ma, 161.5 ±2.4 Ma and 158.4±2.3 Ma, respectively (Fig. 13) are consistent within the analytical uncertainties. Unfortunately, the ages achieved by the different mineral chronometers: zircon for the magmatic episode, monazite, titanite and xenotime for the metamorphic one, between 161 and 158 Ma, are similar within the analytical uncertainties and do not allow to specify the chronology of this cooling from magmatic temperatures to those of the greenschist facies (550–600 °C). This attests that the magmatism and the metamorphism associated with the cooling of the magmatic rock follow one another in a very short time.

The metagabbros also present very low temperature mineral assemblages (Prehnite-pumpellyite facies), such as the fine alteration of plagioclase in epidote and albite (Fig. 7), and maybe the alteration of ilmenite into titanite + rutile (Fig. 9), or else some minerals in tension cracks. We agree with Mevel et al. (1978) and Bertrand et al. (1987) that this very low temperature event is difficult to date. It is still unclear whether they record the end of the cooling of the gabbro, contemporaneously with the serpentinisation of the surrounding peridotites or if they are linked to the obduction of the ophiolite and the alpine collision.

6.2. Modelling the crystallisation and cooling of the (meta)gabbro of Mont Chenaillet

In order to assess the duration of the cooling process, we have established simple conductive thermo-kinetic models to reproduce the thermal evolution obtained with the petrologic study. The aim is to estimate the thermal evolution and the lifespan of the crystallisation and cooling of a 150 m thick gabbroic lens. The key question is: which duration is required to solidify it? We used a transcription for PC of the CONTACT program (Peacock, 1989; Spear, 1989; Spear and Peacock, 1990; Spear et al., 1991) that simulates contact metamorphism by using an explicit finite difference algorithm to solve the one-dimensional heat transfer from an intrusion to the intruded host rock. The model supposes some simplifications: the igneous body is instantaneously intruded and we do not take into account advective heat transfers during the ascent of magma from the underlying reservoir. Heat transfers only proceeds by conduction while hydrothermal circulation in the gabbro (attested by

Table 3

U-Th-Pb dataset for the dated minerals: zircon, titanite, monazite and xenotime obtained by in situ Laser Ablation ICP-MS.

Zircon CH1 analysis	Pb ppm[1]	Th ppm[1]	U ppm[1]	Th/U	^{207}Pb/^{235}U[2]	2 σ absolute ^{207}Pb/^{235}U	^{206}Pb/^{238}U[2]	2 σ absolute ^{206}Pb/^{238}U	error correlation	Age (Ma) ^{206}Pb/^{238}U	2 σ error ^{206}Pb/^{238}U
Zr1/#1	0.4	4.5	12	0.37	0.4028	0.0621	0.02742	0.00141	0.33	174.4	8.9
Zr1/#2	0.3	3.1	10	0.32	0.2533	0.0424	0.02648	0.00117	0.26	168.5	7.4
Zr1/#3	0.3	3.6	12	0.31	0.1757	0.0352	0.02570	0.00117	0.23	163.6	7.4
Zr1/#4	0.3	3.2	9	0.33	0.3510	0.0584	0.02633	0.00138	0.31	167.5	8.7
Zr1/#5	0.3	2.7	10	0.28	0.2336	0.0377	0.02621	0.00111	0.26	166.8	7.1
Zr2/#1	0.6	7.9	19	0.42	0.2786	0.0326	0.02609	0.00099	0.32	166.0	6.1
Zr2/#3	0.3	3.5	11	0.31	0.3246	0.0540	0.02474	0.00135	0.33	157.5	8.5
Zr5/#1	2.4	21	90	0.23	0.2148	0.0130	0.02543	0.00063	0.41	161.9	4.1
Zr5/#2	4.4	65	162	0.40	0.1686	0.0085	0.02530	0.00060	0.47	161.1	3.7
Zr5/#3	2.4	26	94	0.28	0.1752	0.0152	0.02533	0.00072	0.33	161.3	4.5
Zr5/#4	3.1	41	114	0.36	0.2075	0.0156	0.02545	0.00069	0.36	162.0	4.4
Zr4/#1	4.3	56	163	0.35	0.1756	0.0085	0.02536	0.00060	0.49	161.4	3.7
Zr4/#2	3.1	39	114	0.34	0.1927	0.0102	0.02550	0.00060	0.44	162.3	3.8
Zr4/#3	4.2	63	156	0.40	0.1684	0.0084	0.02529	0.00057	0.45	161.0	3.7
Zr4/#4	6.4	106	233	0.45	0.1714	0.0074	0.02520	0.00057	0.52	160.4	3.6
Zr4/#5	4.7	61	171	0.36	0.1992	0.0089	0.02557	0.00060	0.52	162.8	3.7
Zr4/#6	3.4	43	124	0.35	0.2266	0.0108	0.02557	0.00060	0.49	162.8	3.8
Zr4/#7	8.5	69	342	0.20	0.1740	0.0093	0.02528	0.00060	0.44	160.9	3.8
Zr3/#1	3.2	35	124	0.28	0.1946	0.0101	0.02529	0.00060	0.46	161.0	3.8
Zr3/#2	2.2	17	85	0.20	0.1852	0.0131	0.02536	0.00066	0.37	161.5	4.1
Zr3/#4	4.4	20	181	0.11	0.1719	0.0098	0.02532	0.00060	0.41	161.2	3.8
Zr6/#1	18	75	760	0.10	0.1734	0.0067	0.02528	0.00057	0.59	160.9	3.5
Zr6/#2	5.0	71	188	0.38	0.1750	0.0084	0.02531	0.00057	0.47	161.1	3.7
Zr6/#3	5.5	76	205	0.37	0.1704	0.0076	0.02543	0.00057	0.50	161.9	3.6
Zr6/#4	5.2	72	192	0.38	0.1727	0.0092	0.02533	0.00060	0.45	161.2	3.7
Zr6/#5	4.3	59	160	0.37	0.1782	0.0086	0.02549	0.00057	0.46	162.3	3.7
Zr6/#6	6.0	95	219	0.43	0.1767	0.0081	0.02528	0.00057	0.49	160.9	3.6
Zr6/#7	7.5	130	266	0.49	0.1887	0.0088	0.02533	0.00057	0.48	161.3	3.6
Zr6/#8	7.6	47	318	0.15	0.1777	0.0068	0.02520	0.00054	0.56	160.5	3.5
Zr9/#1	15	71	639	0.11	0.1759	0.0073	0.02514	0.00057	0.55	160.1	3.5
Zr9/#2	6.9	48	276	0.18	0.1882	0.0072	0.02532	0.00057	0.59	161.2	3.5
Zr9/#3	6.2	41	247	0.17	0.1904	0.0083	0.02539	0.00057	0.52	161.7	3.6
Zr7/#1	3.0	18	118	0.15	0.1965	0.0129	0.02536	0.00063	0.38	161.4	4.0
Zr7/#2	1.8	12	66	0.19	0.2367	0.0151	0.02562	0.00066	0.40	163.1	4.2
Zr8/#1	0.3	3.0	10	0.31	0.4271	0.0476	0.02636	0.00108	0.37	167.7	6.9

Zircon CH4 analysis	Pb ppm[1]	Th ppm[1]	U ppm[1]	Th/U	^{207}Pb/^{235}U[2]	2 σ absolute ^{207}Pb/^{235}U	^{206}Pb/^{238}U[2]	2 σ absolute ^{206}Pb/^{238}U	error correlation	Age (Ma) ^{206}Pb/^{238}U	2 σ error ^{206}Pb/^{238}U
Zr1#1	0.6	2.8	7.8	0.36	1.1184	0.0779	0.03220	0.00141	0.63	204.3	8.8
Zr1#2	0.5	6.7	14.0	0.48	0.3019	0.0218	0.02712	0.00096	0.49	172.5	6.0
Zr1#3	0.4	5.6	11.2	0.50	0.3270	0.0223	0.02688	0.00093	0.51	171.0	5.9
Zr1#4	0.3	4.1	8.3	0.50	0.1803	0.0197	0.02559	0.00096	0.34	162.9	6.1
Zr1#5	0.3	4.4	8.7	0.51	0.1901	0.0194	0.02522	0.00093	0.36	160.6	5.9
Zr1#6	0.9	16.6	35.2	0.47	0.1682	0.0087	0.02496	0.00078	0.60	158.9	4.8
Zr1#7	1.4	19.5	32.5	0.60	0.6409	0.0255	0.02934	0.00093	0.80	186.4	5.7
Zr1#8	0.8	10.8	26.1	0.41	0.2707	0.0132	0.02652	0.00084	0.65	168.7	5.2
Zr1#9	0.8	14.3	30.3	0.47	0.1912	0.0104	0.02533	0.00078	0.57	161.3	5.0
Zr1#10	1.0	19.0	29.0	0.65	0.3997	0.0165	0.02735	0.00084	0.74	173.9	5.3
Zr1#11	0.7	7.4	21.2	0.35	0.4478	0.0203	0.02808	0.00087	0.68	178.5	5.6
Zr1#12	0.7	10.6	25.5	0.42	0.1816	0.0095	0.02548	0.00078	0.58	162.2	4.9
Zr1#13	0.4	4.5	11.9	0.38	0.4760	0.0285	0.02788	0.00096	0.58	177.3	6.0
Zr1#14	1.0	16.2	25.7	0.63	0.5098	0.0209	0.02820	0.00087	0.75	179.2	5.4
Zr1#15	0.8	17.4	28.6	0.61	0.1723	0.0090	0.02497	0.00075	0.58	159.0	4.8
Zr1#16	0.9	17.4	31.0	0.56	0.1995	0.0097	0.02549	0.00078	0.63	162.3	4.9
Zr1#17	0.8	10.4	17.7	0.59	0.8760	0.0402	0.03113	0.00102	0.71	197.6	6.4

Monazite CH1 analysis	Pb ppm[1]	Th ppm[1]	U ppm[1]	Th/U	^{207}Pb/^{235}U[2]	2 σ absolute ^{207}Pb/^{235}U	^{206}Pb/^{238}U[2]	2 σ absolute ^{206}Pb/^{238}U	error correlation	Age (Ma) ^{206}Pb/^{238}U	2 σ error ^{206}Pb/^{238}U
Mz1	404	25,551	1174	21.8	0.2130	0.0377	0.02658	0.00147	0.31	169.1	9.2
Mz2	622	37,995	1684	22.6	0.2274	0.0173	0.02641	0.00111	0.55	168.0	6.9
Mz3	670	39,293	1963	20.0	0.1849	0.0161	0.02569	0.00108	0.48	163.5	6.8
Mz4	293	17,609	879	20.0	0.2158	0.0229	0.02651	0.00117	0.42	168.7	7.4
Mz5	236	9971	941	10.6	0.5941	0.0425	0.03747	0.00162	0.60	237.2	10.0
Mz6	69	2422	150	16.2	0.7410	0.0921	0.04255	0.00178	0.34	268.6	33.1
Mz7	111	5668	361	15.7	0.3603	0.0517	0.02983	0.00178	0.42	189.5	38.6
Mz8	267	15,412	616	25.0	0.2629	0.0366	0.02782	0.00144	0.37	176.9	29.5
Mz9	487	29,963	1192	25.1	0.2043	0.0228	0.02731	0.00123	0.40	173.7	19.2
Mz10	145	9116	517	17.6	0.3414	0.0494	0.02739	0.00156	0.39	174.2	37.4

(*continued on next page*)

Table 3 (*continued*)

Zircon CH1 analysis	Pb ppm[1]	Th ppm[1]	U ppm[1]	Th/U	$^{207}Pb/^{235}U$[2]	2 σ absolute $^{207}Pb/^{235}U$	$^{206}Pb/^{238}U$[2]	2 σ absolute $^{206}Pb/^{238}U$	error correlation	Age (Ma) $^{206}Pb/^{238}U$	2 σ error $^{206}Pb/^{238}U$
Xenotime CH1 analysis	Pb ppm[1]	Th ppm[1]	U ppm[1]	Th/U	$^{207}Pb/^{235}U$[2]	2 σ absolute $^{207}Pb/^{235}U$	$^{206}Pb/^{238}U$[2]	2 σ absolute $^{206}Pb/^{238}U$	error correlation	Age (Ma) $^{206}Pb/^{238}U$	2 σ error $^{206}Pb/^{238}U$
Xe1	350	662	6294	0.11	0.1702	0.0093	0.02499	0.00099	0.72	159.1	6.2
Xe2	467	1243	8366	0.15	0.1717	0.0088	0.02475	0.00099	0.78	157.6	6.2
Xe3	459	1438	6702	0.21	0.2525	0.0128	0.02851	0.00114	0.79	181.2	7.1
Xe4	414	1066	6692	0.16	0.2133	0.0123	0.02672	0.00108	0.70	170.0	6.7
Xe5	293	1086	4878	0.22	0.1910	0.0123	0.02589	0.00105	0.63	164.7	6.6
Xe6	184	525	2790	0.19	0.2382	0.0221	0.02774	0.00120	0.47	176.4	7.6
Xe7	636	853	8927	0.10	0.3129	0.0197	0.02992	0.00123	0.65	190.1	7.7
Xe8	736	6188	7910	0.78	0.4592	0.0249	0.03425	0.00138	0.74	217.1	8.6
Xe9	400	768	7232	0.11	0.1754	0.0097	0.02569	0.00102	0.72	163.5	8.3
Xe10	281	748	4780	0.16	0.2064	0.0132	0.02621	0.00105	0.63	166.8	11.1
Xe11	315	1065	5574	0.19	0.1816	0.0111	0.02556	0.00102	0.65	162.7	9.5
Xe12	375	1171	6573	0.18	0.1797	0.0110	0.02596	0.00102	0.64	165.2	9.5
Titanite CH1 analysis	Pb ppm[1]	Th ppm[1]	U ppm[1]	Th/U	$^{207}Pb/^{235}U$[2]	2 σ absolute $^{207}Pb/^{235}U$	$^{206}Pb/^{238}U$[2]	2 σ absolute $^{206}Pb/^{238}U$	error correlation	Age (Ma) $^{206}Pb/^{238}U$	2 σ error $^{206}Pb/^{238}U$
Ti1	2.4	90	53	1.68	0.4269	0.0236	0.02683	0.00072	0.49	170.7	4.6
Ti2	2.2	78	53	1.47	0.3675	0.0215	0.02607	0.00072	0.47	165.9	4.4
Ti3	2.9	63	91	0.69	0.2526	0.0145	0.02588	0.00063	0.43	164.7	4.1
Ti4	4.0	123	127	0.96	0.2271	0.0103	0.02534	0.00063	0.55	161.3	3.9
Ti5	2.5	64	70	0.91	0.4026	0.0200	0.02653	0.00072	0.55	168.8	4.5
Ti6	4.3	115	140	0.82	0.2664	0.0128	0.02560	0.00066	0.54	162.9	4.1
Ti7	4.4	72	109	0.66	0.6684	0.0317	0.02857	0.00081	0.60	181.6	5.0
Ti8	4.0	108	115	0.94	0.3511	0.0166	0.02632	0.00069	0.56	167.5	4.3
Ti9	1.0	39	32	1.19	0.2169	0.0257	0.02468	0.00090	0.31	157.2	5.6
Ti10	0.9	48	24	2.02	0.2182	0.0239	0.02502	0.00084	0.31	159.3	5.3

Decay constants of Jaffrey et al. (1971) used.

[1] Concentration uncertainty c.20%.

[2] Data not corrected for common-Pb.

the abundance of hydrated minerals) enables a fast heat transfer (e.g. Zhang et al., 2014). The model assumes a single injection without replenishment of the magmatic lens. In the studied case, this condition seems to be more or less satisfied, as evidenced by the scarcity of intrusive contacts of gabbro in gabbro (Fig. 3), or between the different lithologies: troctolite – gabbro – plagiogranites (diorite and albitites), thus suggesting a limited replenishment or reinjection of the magmatic lens.

Thermodynamic constants have been selected following Spear and Peacock (1990), Cannat et al. (2004), Lesher and Spera (2015) and Gillis and Coogan (2019) with a thermal conductivity of 3.0 W/m/K, a rock density of 3000 kg/m^3, a specific capacity of 1200 J.kg/K and a latent heat of crystallisation of 400 kJ/kg. We set the liquidus at 1200 °C, a realistic temperature for a relatively primitive basaltic melt, and an almost dry solidus around 1050 °C. According to Escartín et al. (2003) and Manatschal et al. (2011) the gabbros are intrusive in very shallow levels in a cold lithosphere at the brittle-ductile transition. If the gabbro is exhumed along an oceanic detachment fault, the temperature of the surrounding rocks has changed progressively during the exhumation since the emplacement in a high temperature environment to the sea-floor. This variation of temperature during the exhumation and the rate of this exhumation will determine the cooling rate of the gabbro. Consequently, we chose an average fixed temperature of 550 °C for the surrounding rocks which corresponds to the estimated temperature of the tiny ductile shear zone containing the three chronometer minerals: titanite, monazite, and xenotime (Fig. 8)

Our straightforward thermal modelling predicts that the magmatic lens is completely solidified in about 350 years and cooled to 550–600 °C in less than 8000 years (Fig. 14). If the cooling started in a warmer environment, in the range of 750–700 °C, and then gradually decreased, this would only change our result by a factor of 3 or 4. However, as already highlighted, the cooling of the Mont Chenaillet gabbro takes place in a context of strong hydrothermal convection and therefore these estimates using such conductive thermal models can only be maximum. These surely greatly overestimate the time of cooling. Nevertheless and despite the uncertainties of this calculation, these models give an order of magnitude of the cooling time of a gabbro massif like that of Mont Chenaillet. They are in agreement with the proposals of Escartín et al. (2003) who suggest that the distribution and duration of gabbro emplacement had to be limited in space and time. Although the cooling rates estimated by Coogan et al. (2007) or Faak and Gillis (2016) are lower than our results, these authors demonstrate that the cooling of gabbros in the oceanic crust is very fast. On the contrary, the cooling rates considered by Zhang et al. (2014) are significantly higher in the context of a vigorous hydrothermal circulation. In a similar way, McCaig et al. (2010) suggest that hydrothermal discharge along detachment fault favours rapid cooling of the gabbros. In all cases, our estimations are far below the analytical uncertainties of our geochronometers and nicely explain why we cannot resolve the different stages of the cooling history ages with this method.

6.3. *Two origins for the sources of water*

The multiple generations of hydrated minerals crystallising throughout the retrograde thermal evolution from the late-magmatic stage (sample CH3: 950 °C) are evidences of a permanent, albeit irregularly distributed, volatile_bearing agent - rock interaction during multiple fluid infiltration events: brown and green amphiboles and the pervasive low temperature alteration of plagioclase to albite + epidote. Another example of water-rock interaction in the Chenaillet massif is the complete transformation of the troctolite olivines to chlorite and tremolite (Fig. 10). Coogan et al. (2001), Pertsev et al. (2015) and Harigane et al. (2019) well summarised the various sources of water that can lead to the hydration of the oceanic crust: (a) a residual hydrous silicate melt derived from the fractionation of basalt, (b) an exsolved magmatic fluids from such a hydrous silicate melt, (c) seawater-derived fluids and finally mixtures of these end-members.

In the gabbroic massif of Mont Chenaillet, the scarcity of the differentiated facies (ferro-gabbros, diorites and plagiogranites) precludes the assumption that water of magmatic origin was the sole cause

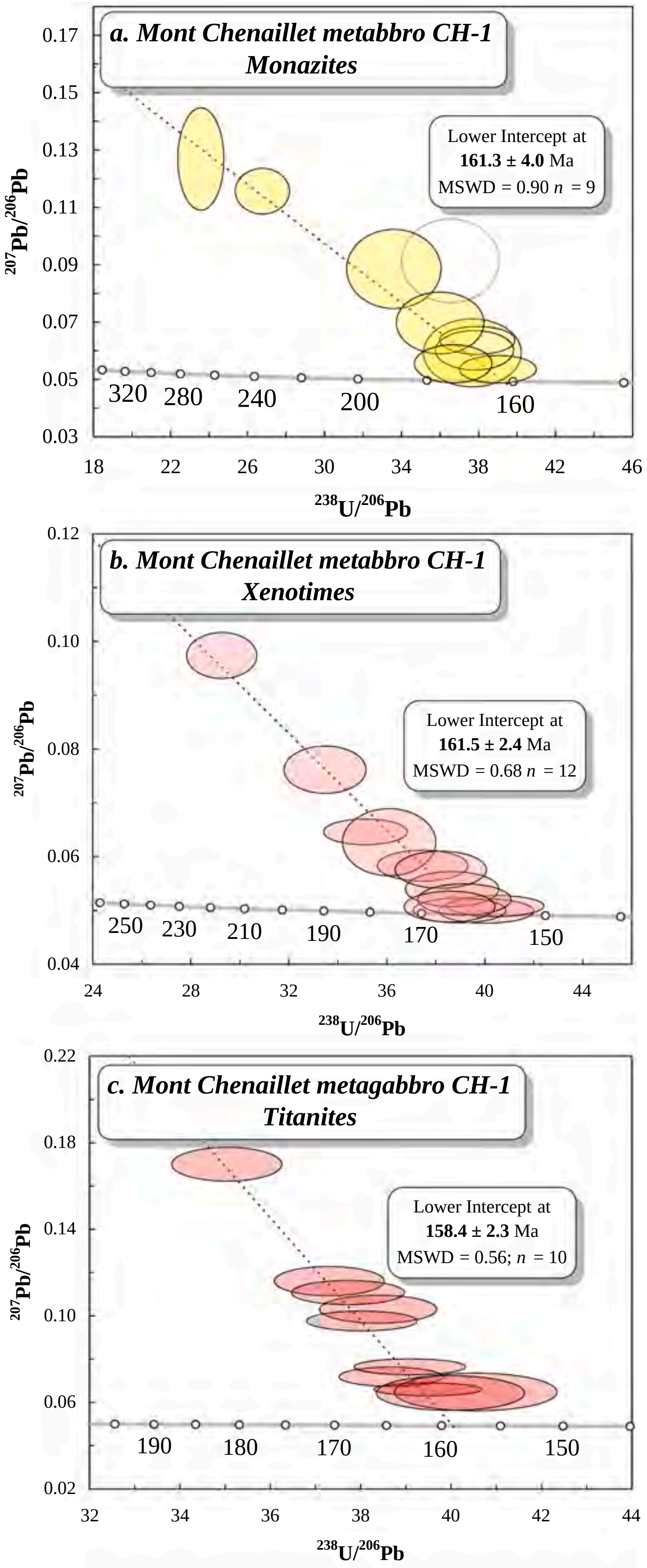

Fig. 13. Geochronological results: Tera–Wasserburg diagram showing the monazite, xenotime and titanite data of the string of titanite +/− ilmenite of CH1 sample.

of the significant hydration of the gabbro lens. On the other hand, the high amount of amphibole in the CH3 sample close to the detachment fault, which represents a preferential channel for the circulation of the seawater, strongly suggests the major role of seawater-derived fluid in the metamorphism of the massif. The extensive alteration of the olivines in the metatroctolites suggests a widespread hydration of these rocks (Fig. 10). However, the detailed study of the chemistry of titanite and the fact that their textural context is linked with very different chemical compositions (Fig. 11) suggest an infiltration of fluids of various nature and hydrous melts. More specifically, type 3 titanite found within a ductile shear in sample CH1 (Fig. 8) have high contents in trace elements (e.g. REE, Nb, Ta, Table 2). Their compositions are characteristics of a felsic melt (Bruand et al., 2014; Hoskin et al., 2000; Prowatke and Klemme, 2005). These signatures of the titanite of the ductile shear are very different from the other titanites both found in CH1 and CH3. Indeed, type 1, 2 and 4 have much lower content in trace elements and REE in particular (Table 2 and Fig 11). Titanite 1 and 2 chemical signatures are inherited from the reaction of previous Ti-bearing phases (Ti-rich Amphibole for type 1 and ilmenite for type 2) and are directly linked to changing metamorphic conditions from granulite toward the amphibolite/greenschist facies. Type 4 was only found in late fractures affecting Ch3 samples and its chemistry (low REE content and positive anomaly) is most likely linked to the late circulation of fluid alterating feldspar. Some authors (eg. Pertsev et al., 2015) have suggested that local enrichment in trace elements of the gabbros (REE, Y, Nb, …) could originate from exsolved magmatic fluids released by hydrous felsic melts such as plagiogranites during their crystallisation. Tribuzio et al., (2019) recently proposed that the small gabbro massif of Rocher de l'Aigle (north of Mont Chenaillet) would be metasomatised by felsic hydrous melt feeding the dykes of albitite. It has to be noted that no intrusive veins at the outcrop scale could be found associated to the micro shear zone in sample CH1 Therefore, instead, the trace element abundance of the type 3 REE-rich titanite (Fig. 11b) in this micro shear zone could originate from a metasomatic fluid resulting from the crystallisation of a SiO_2-rich hydrous melt feeding the veins of albitite and percolated into the already partially cooled gabbro. The varied composition of the other titanite types suggests a diversity of fluid sources. As we are in a context of vigorous hydrothermal circulation in an oceanic crust, a seawater-derived hydrothermal fluid origin of the principal source of water responsible for the overall hydration of the massif is a reasonable hypothesis during the exhumation of the gabbro along the detachment shear zone. Tribuzio et al. (2019) do not preclude such an origin as they write: "we cannot exclude, however, that some of the amphibole (and clinopyroxene) chemical variability reflects replacement and/or overgrowth by a secondary amphibole in response to interaction of the gabbros with fluids, which could be exsolved from the melt trapped within the deformed gabbros, and/or derived from seawater during subsequent exhumation of the gabbros to the seafloor."

7. Conclusions

Multiple generations of metamorphic minerals and specially amphiboles are evidence that the gabbro petrographically records different steps of its cooling during exhumation to the seafloor along an oceanic detachment fault, suggesting that the rock underwent separate episodes of fluid/rock interaction and/or deformation. The timing of this cooling could be theoretically measured using in situ dating on thin section in textural context of the chronometer minerals linked to this metamorphism by LA-ICPMS. The crystallisation age of the gabbro is determined by U—Pb zircon dating at 161.0 +/− 0.8 Ma similar to this obtained in the albitic vein at 161.8 +/− 1.7 Ma, whereas the metamorphic minerals, monazite (161.3 +/− 4.0 Ma), titanite (158.4 ±2.3 Ma) and xenotime (161.5 +/− 2.4 Ma) in a tiny ductile shear zone date a shearing event during the cooling of the gabbro at the transition of the amphibolite and greenschist facies. Unfortunately, the different minerals display similar ages within the analytical uncertainties and the cooling age cannot be distinguished from the magmatic age of the massif. Indeed, a simple numerical model confirms that the crystallisation and cooling of the Mont Chenaillet gabbro are extremely fast: the crystallisation happens in a few hundred years and the cooling is

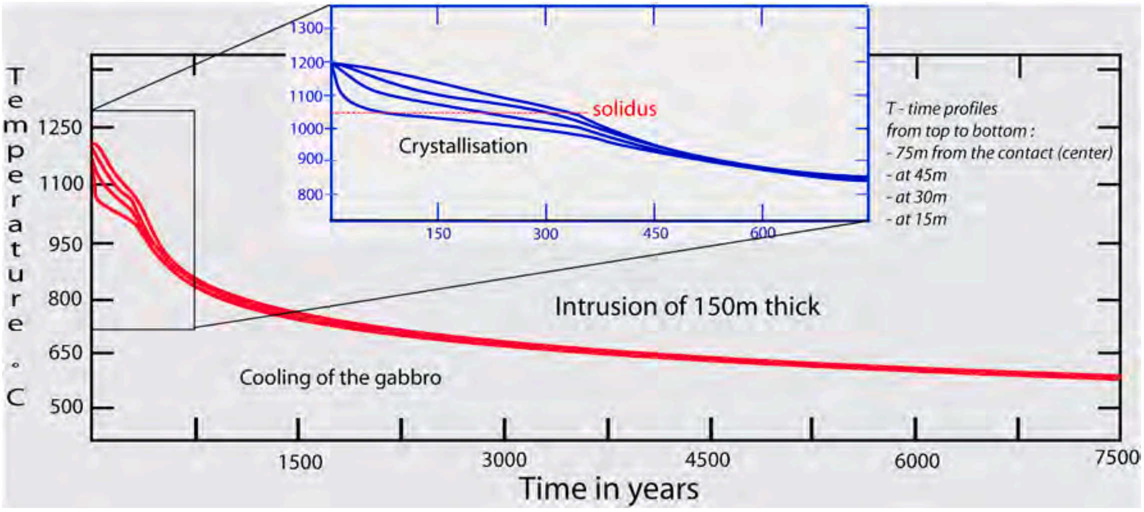

Fig. 14. Thermal modelling: modeled evolution of temperature with time at various points inside a 150 m thick gabbroic lens. From top to bottom, the temperature - time profiles represent respectively the thermal evolution at the center of the intrusion (75 m) and at various distances from the contact, inside the intrusion. In blue: enlargement for the first 750 years, (For interpretation of the references to colour in this figure legend, the reader is referred to the web version of this article.)

completed in a few thousand years. In this way, we show strong evidence for rapid exhumation and cooling of the gabbro related to detachment faults in the Chenaillet ophiolite generated in a slowly spreading accretionary system. Even if the cooling age cannot be resolved with the geochronology, the petrological work and the various chemical compositions recorded in titanite, nicely highlighted that the development of this retrograde metamorphism required multiple fluid (and possibly hydrous SiO2-rich melts) infiltration events enhanced by multiple ductile/brittle deformation events during the exhumation. We propose two origins for the source of water: pervasive seawater-derived fluids and more locally, exsolved magmatic fluids from evolved hydrous silicate melts (plagiogranite veins) and infiltrated into the already partially cooled gabbro. Even if we have no evidence, we cannot exclude that the gabbro could be locally metasomatised by felsic hydrous melt feeding the dykes of albitite as suggested by Tribuzio et al. (2019) in the neighbouring massif.

Supplementary data to this article can be found online at https://doi.org/10.1016/j.lithos.2022.106620.

Declaration of Competing Interest

The authors declare that they have no known competing financial interests or personal relationships that could have appeared to influence the work reported in this paper.

Acknowledgements

The co-Editor-in-Chief Nadia Malaspina, Maria Rosaria Renna and an anonymous reviewer are thanked for their constructive comments. Thanks are due to Jean Luc Devidal for his help in the use of EMPA. This is Laboratory of Excellence ClerVolc contribution number 526.

References

Bertrand, J., Courtin, B., Vuagnat, M., 1982. Elaboration d'un secteur de lithosphère océanique liguro-piémontais d'après les données de l'ophiolite du Montgenèvre (Hautes-Alpes, France et province de Turin). Ofioliti 7, 155–196.

Bertrand, J., Dietrich, V., Nievergelt, P., Vuagnat, M., 1987. Comparative major and trace element geochemistry of gabbroic and volcanic rock sequences, Montgenèvre ophiolite, Western Alps. Schweiz. Mineral. Petrogr. Mitt. 67, 147–169.

Boynton, W.V., 1984. Cosmochemistry of the rare earth elements: meteorite studies. Dev. Geochem. 63–114. https://doi.org/10.1016/b978-0-444-42148-7.

Bruand, E., Storey, C., Fowler, M., 2014. Accessory mineral chemistry of high Ba-Sr granites from Northern Scotland: constraints on petrogenesis and records of whole-rock Signature. J. Petrol. 55, 1619–1651. https://doi.org/10.1093/petrology/egu037.

Caby, R., 1995. Plastic deformation of gabbros in a slow-spreading Mesozoic Ridge: Example of the Montgènevre Ophiolite. In: Vissers, R.L.M., Nicolas, A. (Eds.), Mantle and Lower Crust Exposed in Oceanic Ridges and in Ophiolites. Kluwer Academic Publishers, pp. 123–145.

Canales, J.P., Dunn, R.A., Arai, R., Sohn, R.A., 2017. Seismic imaging of magma sills beneath an ultramafic-hosted hydrothermal system. Geology 45, 451–454. https://doi.org/10.1130/G38795.1.

Cannat, M., Cann, J., Maclennan, J., 2004. Some hard rock constraints on the supply of heat to mid-ocean ridges. Mid-ocean Ridges: Hydrothermal Interactions between the Lithosphere and Oceans. American Geophysical, Washington, DC, pp. 111–149.

Chalot-Prat, F., 2005. An undeformed ophiolite in the Alps: field and geochemical evidence for a link between volcanism and shallow plate tectonic processes. In: Foulger, G.R., Natland, J.H., Presnall, D.C., Anderson, D.L. (Eds.), Plates, Plumes and Paradigms. Geological Society of America Special Papers, 388, pp. 751–780.

Coogan, L.A., Wilson, R.N., Gillis, K.M., MacLeod, C.J., 2001. Near-solidus evolution of oceanic gabbros: insights from amphibole geochemistry. Geochim. Cosmochim. Acta 65, 4339–4357.

Coogan, L.A., Wilson, R.N., Jenkin, G.R.T., 2007. Contrasting cooling rates in the lower oceanicCrust at fast- and slow-spreading ridges revealed by geospeedometry. J. Petrol. 48, 2211–2231.

Cordey, Fabrice, Bailly, Anthony, 2007. Alpine Ocean seafloor spreading and onset of pelagic sedimentation: new radiolarian data from the Chenaillet-Montgenèvre ophiolite (French-Italian Alps). Geodin. Acta 20 (3), 131–138. https://doi.org/10.3166/ga.20.131-138.

Corfu, Fernando, Hanchar, John M., Hoskin, Paul W.O., Kinny, Peter, 2003. Atlas of zircon textures. Rev. Mineral. Geochem. 53 (1), 469–500. https://doi.org/10.2113/0530469.

Costa, S., Caby, R., 2001. Evolution of the Ligurian Tethys in the Western Alps: Sm/Nd and U/Pb geochronology and rare-earth element geochemistry of the Montgenèvre ophiolite (France). Chem. Geol. 175, 449–466.

Desmurs, L., Müntener, O., Manatschal, G., 2002. Onset of magmatic accretion within a magma-poor rifted margin: a case study from the Platta Ocean-continent transition, eastern Switzerland. Contrib. Mineral. Petrol. 144 (3), 365–382.

Ernst, W.G., Liu, J., 1998. Experimental phase-equilibrium study of Al- and Ti-contents of calcic amphibole in MORB—A semiquantitative thermobarometer. Am. Mineral. 83 (9–10), 952–969. https://doi.org/10.2138/am-1998-9-1004.

Escartín, J., Mevel, C., MacLeod, C.J., McCaig, A.M., 2003. Constraints on deformation conditions and the origin of oceanic detachments: the Mid-Atlantic Ridge core complex at 15°45′N. Geochem. Geophys. Geosyst. 4, 1067. https://doi.org/10.1029/2002GC000472.

Faak, K., Gillis, K., 2016. Slow cooling of the lowermost oceanic crust at the fast-spreading East Pacific rise. Geology 44, 115–118. https://doi.org/10.1130/G37353.1.

Fallourd, S., Poujol, M., Boulvais, P., Paquette, J.L., de Saint Blanquat, M., Rémy, P., 2014. In situ LA-ICP-MS U-Pb titanite dating of Na-Ca metasomatism in orogenic belts : the North Pyrenean example. Int. J. Earth Sci. 103, 667–682.

France, L., Lombard, M., Nicollet, C., Berthod, C., Debret, B., Koepke, J., Ildefonse, B., Toussaint, A., 2021. Quantifying the axial magma lens dynamics at the roof of oceanic magma reservoirs (dike / gabbro transition): Oman Drilling Project GT3 site survey. J. Geophys. Res. Solid Earth. https://doi.org/10.1029/2020JB021496.

Gillis, K.M., Coogan, L.A., 2019. A review of the geological constraints on the conductive boundary layer at the base of the hydrothermal system at mid-ocean ridges. Geochem. Geophys. Geosyst. 20, 67–83. https://doi.org/10.1029/2018gc007878.

Gonçalves, G.O., Cristiano Lana, C., Scholz, R., Buick, I.S., Gerdes, A., Kamo, S.L., Corfu, F., Marinho, M.M., Chaves, A.O., Valeriano, C., NaliniJr., H.A., 2016. An assessment of monazite from the Itambé pegmatite district for use asU–Pb isotope reference material for microanalysis and implications forthe origin of the"Moacyr" monazite. Chem. Geol. 424 (30), 50.

Griffin, W., 2008. GLITTER: Data Reduction Software for Laser Ablation ICP-MS. Laser Ablation ICP-MS in the Earth Sciences: Current Practices and Outstanding Issues, pp. 308–311.

Harigane, et al., 2019. Melt–fluid infiltration along detachment shear zones in oceanic core complexes: Insights from amphiboles in gabbro mylonites from the Godzilla Megamullion, Parece Vela Basin, the Philippine Sea. Lithos 344–345, 217–231.

Heaman, L.M., 2009. The application of U–Pb geochronology to mafic, ultramafic and alkaline rocks: an evaluation of three mineral standards. Chem. Geol. 261, 43–52. https://doi.org/10.1016/j.chemgeo.2008.10.021.

Hiess, J., Condon, D.J., McLean, N., Noble, S.R., 2012. $^{238}U/^{235}U$ systematics in terrestrial uranium-bearing minerals. Science 335, 1610–1614.

Holland, T., Blundy, J., 1994. Non-ideal interactions in calcic amphiboles and their bearing on amphibole-plagioclase thermometry. Contr. Mineral. and Petrol. 116, 433–447. https://doi.org/10.1007/BF00310910.

Hoskin, P.W.O., PD, Kiinny, Wyborn, D., Chappell, B.W., 2000. Identifying AccessorL Mineral Saturation during Differentiation in Granitoid Magmas: an Integrated Approach. J. Petrol. 41, 1365–1396. https://doi.org/10.1093/petrology/41.9.1365.

Hurai, V., Paquette, J.L., Huraiová, M., Konečný, P., 2010. Age of deep crustal magmatic chambers in the intra-Carpathian back-arc basin inferred from LA-ICPMS U-Th-Pb dating of zircon and monazite from igneous xenoliths in alkali basalts. J. Volcanol. Geotherm. Res. 198, 275–287.

Jackson, S.E., Pearson, N.J., Griffin, W.L., Belousova, E.A., 2004. The application of laser ablation-inductively coupled plasma-mass spectrometry to in situ U–Pb zircon geochronology. Chem. Geol. 211, 47–69.

Jaffrey, A.H., Flynn, K.F., Glendenin, L.E., Bentley, W.C., Essling, A.M., 1971. Precision measurement of half-lives and specific activities of ^{235}U and ^{238}U. Phys. Rev. C4,, 1889–1906.

Jochum, K.P., Willbold, M., Raczek, I., Stoll, B., Herwig, K., 2005. Chemical Characterisation of the USGS Reference Glasses GSA-1G, GSC-1G, GSD-1G, GSE-1G, BCR-2G, BHVO-2G and BIR-1G using EPMA, ID-TIMS, ID-ICP-MS and LA-ICP-MS. Geostand. Geoanal. Res. 29, 285–302.

Leake, B.E., Woolley, A.R., Arps, C.E.S., Birch, W.D., Gilbert, M.C., Grice, J.D., Hawthorne, F.C., Kato, A., Kisch, H.J., Krivovichev, V.G., Linthout, K., Laird, J., Mandarino, J.A., Maresch, W.V., Nickel, E.H., Rock, N.M.S., Schumacher, J.C., Smith, D.C., Stephenson, N.C.N., Ungaretti, L., Whittaker, E.J.W., Guo, Y., 1997. Nomenclature of amphiboles: report of the subcommittee on amphiboles of the International Mineralogical Association, Commission on New Minerals and Mineral Names. Can. Mineral. 35, 219–246.

Lesher, C.E., Spera, F.J., 2015. Thermodynamic and Transport Properties of Silicate Melts and Magma. Academic Press, Elsevier. The encyclopedia of volcanoes, pp. 113–141.

Li, X.H., Faure, M., Lin, W., Manatschal, G., 2013. New isotopic constraints on age and magma genesis of an embryonic oceanic crust: the Chenaillet Ophiolite in the Western Alps. Lithos 160-161, 283–291. https://doi.org/10.1016/j.lithos.2012.12.016.

Ludwig, K.R., 2001. User's Manual for Isoplot/Ex Version 2.49, A Geochronological Toolkit for Microsoft Excel. Berkeley Geochronological Center, Special Publication 1a, Berkeley, USA, 55 pp.

Manatschal, G., Müntener, O., 2009. A type sequence across an ancient magma-poor ocean–continent transition: the example of the western Alpine Tethys ophiolites. Tectonophysics 473, 4–19. https://doi.org/10.1016/j.tecto.2008.07.021.

Manatschal, G., Sauter, D., Karpoff, A.M., Masini, E., Mohn, G., Lagabrielle, Y., 2011. The Chenaillet Ophiolite in the French/Italian Alps: an ancient analogue for an Oceanic Core complex? Lithos 124, 169–184.

McCaig, A.M., Delacour, A., Fallick, A.E., Castelain, T., Früh-Green, G.L., 2010. Detachment fault control on hydrothermal circulation systems: Interpreting the subsur-face beneath the TAG hydrothermalfield using the isotopic and geologicalevolution of oceanic core complexes in the Atlantic. In: Rona, P.A., et al. (Eds.), Diversity of Hydrothermal Systems on Slow Spreading Ocean Ridges. Geophysical Monograph, 188. American Geophysical Union, Washington DC, pp. 207–239. https://doi.org/10.1029/2008GM000729.

McCarthy, A., Tugend, J., Mohn, G., 2021. Formation of the Alpine Orogen by amagmatic convergence and assembly of previously rifted lithosphere. Elements 17, 29–34. https://doi.org/10.2138/gselements.17.1.29.

Mevel, C., Caby, R., Kienast, J.-R., 1978. Amphibolite facies conditions in the oceanic crust: example of amphibolitized flaser-gabbro and amphibolites from the Chenaillet ophiolite massif (Hautes Alpes, France). Earth Planet. Sci. Lett. 39 (1), 98–108. https://doi.org/10.1016/0012-821x(78)90146-2.

Molina, J.F., Cambeses, A., Moreno, J.A., Morales, I., Montero, P., Bea, F., 2021. A reassessment of the amphibole-plagioclase NaSi-CaAl exchange thermometer with applications to igneous and high-grade metamorphic rocks. Am. Mineral. 106, 782–800. https://doi.org/10.2138/am-2021-7400.

Otten, M.T., 1984. The origin of brown hornblende in Artfjallet gabbro and dolerites. Contrib. Mineral. Petrol. 86, 189–199.

Paquette, J.L., Piro, J.L., Devidal, J.L., Bosse, V., Didier, A., 2014. Sensitivity enhancement in LA-ICP-MS by N2 addition to carrier gas: application to radiometric dating of U-Th-bearing minerals. Agil. ICP-MS J. 58, 4–5.

Paquette, J.L., Ballèvre, M., Peucat, J.J., Cornen, G., 2017. From opening to subduction of an oceanic domain constrained by LA-ICP-MS U-Pb zircon dating (Variscan belt, Southern Armorican Massif, France). Lithos 294-295, 418–437.

Peacock, S.M., 1989. Thermal modeling of metamorphic pressure-temperature-time paths: A forward approach. In: Spear, F.S., Peacock, S.M. (Eds.), Metamorphic Pressure-Temperature-Time Paths. AGU, Washington, D. C, pp. 57–102. Short Course in Geology, 7.

Pertsev, A.N., Aranovich, L.Y., Prokofiev, V.Y., Bortnikov, N.S., Cipriani, A., Simakin, S. S., Borisovskiy, S.E., 2015. Signatures of residual melts, magmatic and seawater-derived fluids in oceanic lower-crust gabbro from the Vema lithospheric section, Central Atlantic. J. Petrol. 56, 1069–1088. https://doi.org/10.1093/petrology/egv028.

Prowatke, S., Klemme, S., 2005. Effect of melt composition on the partitioning of trace elements between titanite and silicate melt. Geochim. Cosmochim. Acta 69, 695–709. https://doi.org/10.1016/j.gca.2004.06.037.

Putirka, K., 2016. Amphibole thermometers and barometers for igneous systems and some implications for eruption mechanisms of felsic magmas at arc volcanoes. Am. Mineral. 101 (4), 841–858.

Rampone, E., Sanfilippo, A., 2021. The heterogeneous Tethyan oceanic lithosphere of the Alpine ophiolites. Elements 17, 23–28. https://doi.org/10.2138/gselements.17.1.23.

Spear, F.S., 1989. Petrologic determination of metamorphic pressure-temperature-time paths. In: Spear, F.S., Peacock, S.M. (Eds.), Metamorphic Pressure-Temperature-Time Paths, Short Course in Geology. American Geophysical Union, Washington, DC, pp. 1–55.

Spear, F.S., Peacock, S.M., 1990. Metamorphic P-T-T Paths: Program Manual and Computer Exercises for the Calculation of Metamorphic Phase Equilibria, Pressure-Temperature-Time Paths and Thermal Evolution of Orogenic Belts. Geological Society of America short course, Dallas, Texas, p. 188.

Spear, F.S., Peacock, S.M., Kohn, M.J., Florence, F.P., Menard, T., 1991. Computer programs for petrologic PTt path calculations. Amer. Mineral. 76 (11–12), 2009–2012.

Tera, F., Wasserburg, G.J., 1972. U-Th-Pb systematics in three Apollo 14 basalts and the problem of initial Pb in lunar rocks. Earth Planet. Sci. Lett. 14, 281–304.

Tomascak, P.B., Krogstad, E.J., Walker, R.J., 1996. U-Pb Monazite Geochronology of Granitic Rocks from Maine: implications for Late Paleozoic Tectonics in the Northern Appalachians. J. Geol. 104, 2.

Tribuzio, R., Garzetti, F., Corfu, F., Tiepolo, M., Renna, M.R., 2016. U–Pb zircon geochronology of the Ligurian ophiolites (Northern Apennine, Italy): implications for continental breakup to slow seafloor spreading. Tectonophysics 666, 220–243. https://doi.org/10.1016/j.tecto.2015.10.024.

Tribuzio, R., Manatschal, G., Renna, M.R., Ottolini, L., Zanetti, A., 2019. Tectono-magmatic interplay and related metasomatism in gabbros from the Chenaillet ophiolite (Western Alps). J. Petrol. 60, 2483–2508. https://doi.org/10.1093/petrology/egaa015.

van Achterbergh, E., Ryan, C.G., Jackson, S.E., Griffin, W., 2001. Data reduction software for LA-ICP-MS. In: Sylvester, P. (Ed.), Laser Ablation-ICPMS in the Earth Sciences, 29. Mineralogical Association of Canada, pp. 239–243.

Whitney, D.L., Evans, B.W., 2010. Abbreviations for names of rock-forming minerals. Am. Mineral. 95, 185–187. https://doi.org/10.2138/am.2010.3371.

Wiedenbeck, M., Allé, P., Corfu, F., Wl, Griffin, Meier, M., Oberli, F., Quadt, A.V., Roddick, J.C., Spiegel, W., 1995. Three natural zircon standards for U-Th-Pb, Lu-Hf, trace element and REE analyses. Geostand. Newslett. 19, 1–23.

Zhang, C., Koepke, J., Kirchner, C., Götze, N., Behrens, H., 2014. Rapid hydrothermal cooling above the axial melt lens at fast-spreading mid-ocean ridge. Sci. Rep. 4, 6342. https://doi.org/10.1038/srep06342.